AGU ADVANCING EARTH AND SPACE SCIENCES

Earth's Future

Key Points:
- Reduced anthropogenic aerosol emissions lead to a global-scale increase in boreal summer rainfall in the mid-21st century
- Decreased greenhouse gas emissions under green scenario induce reduction in boreal summer rainfall around the world in the mid-21st century
- Simultaneous reductions in aerosol and greenhouse gas emissions induce amplified interhemispheric rainfall contrast in the mid-21st century

Correspondence to:
H. Zhang,
huazhang@cma.gov.cn

Amplified Interhemispheric Rainfall Contrast in Boreal Summer Due To Reduction in Anthropogenic Emissions Under COVID-MIP Green Economic-Recovery Scenarios

Xiaochao Yu[1,2], Hua Zhang[1,3] [ID]**, Bing Xie[4], and Piers M. Forster[5]** [ID]

[1]State Key Laboratory of Severe Weather, Chinese Academy of Meteorological Sciences, Beijing, China, [2]Department of Atmospheric and Oceanic Sciences, Institute of Atmospheric Sciences, Fudan University, Shanghai, China, [3]Collaborative Innovation Center on Forecast and Evaluation of Meteorological Disasters, Nanjing University of Information Science and Technology, Nanjing, China, [4]Laboratory for Climate Studies, National Climate Center, China Meteorological Administration, Beijing, China, [5]Priestley International Centre for Climate, University of Leeds, Leeds, UK

Abstract Our study looks at the precipitation responses to two possible future emission-mitigation pathways, pushed by the Coronavirus Disease 2019 pandemic (COVID-19) and achieving carbon neutrality in the mid-21st century. We find that a simultaneous-reduction in well-mixed greenhouse gases (WMGHGs) and anthropogenic aerosol emissions results in an enhanced interhemispheric precipitation contrast in the 2040s by amplifying the interhemispheric thermal contrast and strengthening the meridional overturning circulation in the tropics. Reduced aerosol emissions induce generally-increased precipitation in the Northern Hemisphere (NH) and an amplified intertropical rainfall contrast, while reduced WMGHG emissions dominate decrease in precipitation in the areas away from aerosol emission sources. Further, the above precipitation contrast will be enhanced under stronger emission-mitigation pathways, mainly attributed to larger precipitation increases in the NH caused by reduced aerosols. More aggressive WMGHGs mitigation policies are necessary to counteract the aerosol-induced warming in the NH, thereby mitigating the risk of regional drying or wetting due to the asymmetry in interhemispheric energy budgets.

Plain Language Summary Under the background that most countries around the world have made carbon-neutral commitments to pursue the 1.5°C warming limit and mitigate climate change, the emergence and persistence of the Coronavirus Disease 2019 (COVID-19) pandemic has provided a unique opportunity to investigate the impacts of anthropogenic emissions mitigation on climate. In this study we estimated the changes in boreal summer rainfall due to reductions in emissions of anthropogenic forcing agents, such as WMGHGs and aerosols, under the latest COVID-19 green economic-recovery scenarios using an aerosol-climate coupled model. We find that reductions in aerosol emissions induce generally increased precipitation in the Northern Hemisphere (NH) and decreased precipitation at low latitudes of the Southern Hemisphere (SH), while reduced WMGHG emissions dominate decreases in precipitation over the SH middle latitudes. The comprehensive effect of simultaneous decreases in anthropogenic emissions may lead to more abundant summer rainfall in the NH, while drier winters in the SH. Urgent mitigation actions of WMGHGs and aerosols are of course needed to limit widespread climate impacts and improve air quality. In pursuing such pathways, we need to factor their specific climate response into adaptation plans to build climate resilience and pathway-appropriate adaptation policies.

1. Introduction

Since the 1950s, an asymmetric precipitation trend between the two hemispheres, resulting from the weakening of the Asian summer monsoon circulation and a southward shift of the intertropical convergence zone (ITCZ), occurred at the tropical/subtropical areas, putting stress on socioeconomic conditions, agricultural practices, and human lives within the above regions (Chung & Soden, 2017; Ding et al., 2008; Singh, 2016; X. Zhang et al., 2007; L. Zhang & Zhou, 2011). Previous studies have emphasized the key roles of both asymmetric inter-hemispheric energy budgets and the weakening of the land-ocean thermal contrast in driving this asymmetric regional precipitation trend in the tropical and subtropical areas (Ding et al., 2009; Marshall et al., 2014; Schneider et al., 2014). Radiative forcings, including that from well-mixed greenhouse gases (WMGHGs) and

anthropogenic aerosols, have considerable impacts on Earth's energy budget, further modifying the rain belt distribution via slow oceanic responses (Lau & Kim, 2017; S. Zhao & Suzuki, 2019).

The WMGHG-driven warming increases atmospheric moisture, contributing to wet regions becoming wetter while dry regions become drier, basically over the oceans (Chou et al., 2007, 2009; Douville et al., 2021; Held & Soden, 2006; Wentz et al., 2007). Greater warming over land than ocean can contribute to regional droughts in subtropical and extratropical land resulting from reductions in continental near-surface relative humidity and a weakening of tropical circulation (Collins et al., 2013; Cook et al., 2019; Lau & Kim, 2017; Plesca et al., 2018; L. Zhang & Li, 2016; W. Zhou et al., 2019). Studies have also demonstrated the key role of aerosols rather than WMGHGs in regulating rainfall trends on regional scales, for example, for the Asian monsoon region (Kishore et al., 2022; Monerie et al., 2022; Song et al., 2014; L. Zhang & Li, 2016). By scattering solar radiation directly or indirectly, aerosols mainly cause prominent surface cooling over the NH continents, damping the land-sea and interhemispheric thermal contrasts (Boucher et al., 2013; Chu et al., 2018; Rosenfeld et al., 2014). This damping effect contributes to the weakening of the Asian monsoon circulation and a southward migration of the ITCZ, resulting in redistributions of boreal summer rainfall (Hwang et al., 2013; S. Zhao & Suzuki, 2019). The contrasting effects of aerosols and WMGHGs on Earth's radiation budgets (Forster et al., 2021), together with the similar roles of them in weakening the thermally driven monsoon circulation (Singh, 2016; W. Zhou et al., 2019), pose challenges for attributing and projecting boreal summer rainfall variations on both global and regional scales.

At present, the emergence and persistence of the Coronavirus Disease 2019 (COVID-19) pandemic has provided an opportunity to investigate the impacts of decreased anthropogenic forcing agents on land-ocean and interhemispheric energy balances and the resulting rainfall redistribution. To stop the spread of COVID-19, strict lockdown measures were implemented worldwide from mid-March to June 2020, leading to a sharp drop in anthropogenic emissions of WMGHGs, aerosols, and their precursors (Le Quéré et al., 2020; Zheng et al., 2020). This decrease in emissions has already been confirmed as an important contributor to the extreme summer precipitation observed in 2020 at the regional scale, for example, an enhanced amount of rainfall by 4% over the Indian landmass (Fadnavis et al., 2021), and explaining about one-third of the observed increase in summer precipitation extremes in eastern China (Yang et al., 2022). Modeling evidence has also suggested that the decreased anthropogenic aerosol emissions related to COVID-19 containment induce enhanced Asian summer monsoon in both 2020 and 2021 by amplifying the land-sea thermal contrast and enhancing the monsoon flow (C. He et al., 2022; Kripalani et al., 2022). More importantly, stronger climate responses, such as the large-scale circulation changes conducive to extreme rainfall production, may occur continuously if anthropogenic emissions keep changing in response to the post-pandemic economic stimulus policies (Forster et al., 2020; Hepburn et al., 2020; Yang et al., 2020; Yu et al., 2022). Therefore, the Coupled Model Intercomparison Project Phase 6 (CMIP6) has introduced a new project (COVID-MIP), which explores the impacts on current and future climate changes from the COVID-19-associated anthropogenic emission adjustments by forcing different models with the same newly-modified emissions pathways (Lamboll et al., 2021).

This study aims to evaluate the responses of boreal summer rainfall during the period of 2020–2050 to persistent anthropogenic emission reductions by putting two green economic-recovery scenarios provided by COVID-MIP (the moderate green and strong green economic-recovery (SGR) scenarios; Lamboll et al., 2021) into an aerosol-climate coupled model. The rest of this paper is organized as follows. Section 2 introduces the COVID-MIP-provided green economic-recovery scenarios, the model used, and experiment design. The responses of boreal summer rainfall to reductions in anthropogenic forcings and the underlying mechanisms are analyzed in Section 3 and discussed in Section 4. The conclusions are provided in Section 5.

2. Methodology

2.1. Green Economic-Recovery Scenarios in COVID-MIP

The COVID-MIP protocol uses two green economic-recovery scenarios, that is, the moderate green economic-recovery (MGR) and SGR scenarios, for investigating the global and regional climate changes induced by decreasing anthropogenic emissions (Lamboll et al., 2021). These COVID-MIP green economic-recovery scenarios assume increased clean energy investment by 0.8% and 1.2%, respectively, relative to the pre-COVID-19 current policy scenario, and project potential emissions levels on the basis of the projected gross domestic product pathways as well as the relationship between low-carbon investment and emissions intensity of the economy

(Climate Action Tracker, 2020; McCollum et al., 2018). The above highly idealized assumptions for the MGR and SGR scenarios result in decreases of WMGHG emissions of about 35% and slightly larger than 50%, respectively, in 2030 compared with the baseline pathway, and achieve net zero carbon dioxide (CO_2) emissions worldwide in 2060 and 2050 (Forster et al., 2020). Such a rate of decrease is in accordance with the 1.5°C Paris Agreement goal (Röser et al., 2020). More details in respect to the COVID-MIP green economic-recovery pathways can refer to Forster et al. (2020).

Meanwhile, the Shared Socioeconomic Pathway (SSP) 2-4.5 emissions scenario was employed by the COVID-MIP protocol as the baseline scenario. The SSP2-4.5 scenario has been applied widely to project future climate changes over decadal to inter-decadal scales due to its central pathway assumption with no substantial deviations and its low to moderate emissions levels (O'Neill et al., 2016). Therefore, we downloaded the SSP2-4.5 data sets from the input data sets for Model Intercomparison Projects (Input4MIPs, 2021). These data sets include the WMGHGs (e.g., CO_2, methane [CH_4], and nitrous oxide [N_2O]) concentration data, and the emission data of aerosols (e.g., sulfates [SF], black carbon [BC], and organic carbon [OC]) and their precursors (e.g., sulfur dioxide). Then the COVID-MIP green economic-recovery scenarios were obtained via modifying gridded projections under the SSP2-4.5 scenario with the appropriate emissions assumptions (Lamboll et al., 2021).

As shown in Figure S1 in Supporting Information S1, upward trends of 7.1% and 1.6% per decade in CO_2 and N_2O concentrations, respectively, occur under the baseline scenario, whereas the CH_4 concentration falls by −1.8% per decade. Under the MGR (SGR) scenario, the actual concentrations of these major WMGHGs decrease markedly compared with the baseline case, with reductions in CO_2, CH_4, and N_2O by 11.5% (15.2%), 15.9% (26.4%), and 1.3% (3%), respectively, in 2050. In contrast to the increase in CO_2 concentration, a persistent drop in atmospheric content of anthropogenic aerosols occurs during 2020–2050 under the baseline scenario (Figure S2 in Supporting Information S1). The decreases in anthropogenic aerosols are much stronger under the COVID-MIP green economic-recovery scenarios, with decreases of −44.3% (−45.1% to −43.6%) and −58% (−58.7% to −57.3%) in anthropogenic aerosol column burdens and reductions of −53.6% (−54.6% to −52.6%) and −66.6% (−67.5% to −65.8%) in anthropogenic aerosol optical depths, respectively, in 2050 relative to the baseline case. These decreases can be attributed to regional drops in the atmospheric content of anthropogenic aerosols in areas with intensive human activities, including East Asia, South Asia, Africa, as well as North America (Figures S3b, S3c, S3e, and S3f in Supporting Information S1).

2.2. Model and Experiments

In this study, we employed the BCC_AGCM2.0_CUACE/Aero model, and this aerosol-climate coupled model was developed by Z. Wang et al. (2014), H. Zhang et al. (2014) and H. Zhang, Wang, et al. (2012). The BCC_AGCM2.0_CUACE/Aero model's atmospheric component, that is, the Atmospheric General Circulation Model of the Beijing Climate Center version 2.0 (BCC_AGCM2.0), was developed by the Beijing Climate Center (BCC) of the Chinese Meteorological Administration (CMA) (Wu et al., 2010). BCC_AGCM2.0 is on the basis of the Eulerian spectral formulation of dynamic equations, employing a horizontal T42 spectral resolution (approximately 2.8° × 2.8°). The vertical resolution of BCC_AGCM2.0 is based on a terrain-following hybrid σ-pressure vertical coordinate, with 26 layers and a rigid lid at about 2.9 hPa. BCC_AGCM2.0 was improved by introducing the new BCC radiation transfer model (BCC_RAD) and the Monte Carlo independent column approximation cloud vertical overlap scheme (Jing et al., 2016; H. Zhang, 2016; H. Zhang et al., 2014). In addition, the optical properties of water and ice clouds, used for radiation calculations by the BCC_RAD, were taken from Nakajima et al. (2000) and H. Zhang et al. (2015), respectively. These schemes help to improve the model's accuracy in simulating seasonal variations in sub-grid cloud structure and the resulting cloud radiative effects. As a result, the above improvements apparently reduce the model biases in respect to radiative fluxes at both the top of the atmosphere and the surface.

An aerosol chemistry model, namely the CMA Unified Atmospheric Chemistry Environment for Aerosol model (CUACE/Aero), was included that considers aerosol emissions, transport, chemical conversion, interactions with clouds and sedimentation processes for five aerosol species, that is, SF, BC, OC, sand/dust (SD), and sea salt (C. Zhou et al., 2012). Among these five aerosol species, emissions of the first three components, and their precursors are prescribed, while the other components are calculated online (Gong et al., 2002, 2003). Each type of aerosols in the CUACE/Aero model is assigned into 12 consecutive bins with non-overlapping, as a geometric series for radii ranging from 0.005 to 20.48 μm. This process helps the CUACE/Aero model to precisely characterize the

Table 1
Experimental Design

Group name	Experiment name	Period	Emission data	Ocean boundary condition
CLIM_All	CLIM_All_ssp2-4.5	2020–2050	SSP2-4.5	Slab ocean model
	CLIM_All_M		Moderate green economic-recovery (both WMGHG and aerosol)	
	CLIM_All_S		Strong green economic-recovery (both WMGHG and aerosol)	
CLIM_Aero	CLIM_Aero_M		Moderate green economic-recovery (only aerosol)	
	CLIM_Aero_S		Strong green economic-recovery (only aerosol)	
CLIM_GHG	CLIM_GHG_M		Moderate green economic-recovery (only WMGHG)	
	CLIM_GHG_S		Strong green economic-recovery (only WMGHG)	

concentrations and optical properties of each type of aerosols with various particle sizes, thereby accurately capturing the anthropogenic aerosol forcings on climate changes. Aerosol optical properties are taken from H. Zhang, Shen, et al. (2012). Moreover, the BCC_AGCM2.0_CUACE/Aero model employs a two-moment cloud microphysical scheme to improve the aerosol-cloud interaction processes (Gettelman et al., 2008; Morrison & Gettelman, 2008; Z. Wang et al., 2014). This scheme allows the BCC_AGCM2.0_CUACE/Aero model to physically represent the direct, semi-direct, and indirect effects of aerosols on liquid-phase clouds, and thereby ensures its simulations of liquid water path, cloud radiative effects, and precipitation to much more agreement with observations.

The BCC_AGCM2.0_CUACE/Aero model has participated successively in several international comparisons, such as AeroCom Phase II and CMIP5, and shown reliable simulations of the spatio-temporal patterns of both the meteorological field and aerosols (Myhre et al., 2013; T. Zhou et al., 2014). This model has been widely employed by researchers to study aerosol radiative forcings and their impacts on monsoon circulation, precipitation redistributions, and the global and regional terrestrial aridity trends (Z. Wang et al., 2015; H. Zhang et al., 2016; S. Zhao et al., 2017).

This study performed three groups of experiments, namely CLIM_All, CLIM_Aero, and CLIM_GHG, which used the same model settings except for forcing pathways (Table 1). There were three experiments in the CLIM_All group. Each experiment contained 10 members with different initial atmospheric conditions to minimize disturbances associated with internal climate variability. The first experiment employed the SSP2-4.5 scenario (CLIM_All_ssp2-4.5), while the latter two experiments used the two COVID-MIP green economic-recovery pathways, namely the moderate green recovery (CLIM_All_M) and the strong green recovery (CLIM_All_S) experiment. The above experiments were driven by the simultaneous variations of WMGHG concentrations and aerosol emissions. The CLIM_Aero and CLIM_GHG groups consisted of two experiments driven solely by aerosol and WMGHG forcings, respectively, corresponding to the two COVID-MIP green economic-recovery scenarios. The other model settings used in these experimental groups were consistent with those in the CLIM_All group. All simulations were 31-year transient runs employing the BCC_AGCM2.0_CUACE/Aero model coupled with a slab ocean model (Hansen et al., 1984). The above slab ocean model considers the effects on ocean temperatures and ice cover from the energy exchange between the atmosphere and ocean, the ocean mixed layer heat capacity, and ocean heat transport (Hansen et al., 1984), and thereby provides physical representations of oceanic boundary conditions to the BCC_AGCM2.0_CUACE/Aero model. The BCC_AGCM2.0_CUACE/Aero model system with a slab ocean has been validated by S. Zhao et al. (2014, 2017). This coupling allows the ocean feedbacks on forcing agent concentrations evolving from 2020 to 2050, as well as the comprehensive and relative contributions of forcing agents with various lifetimes to the spatiotemporal distribution of boreal summer rainfall, to be assessed.

We first assessed the performance of the BCC_AGCM2.0_CUACE/Aero model in simulating the precipitation field under the baseline scenario (details are shown in Section 2.3), by comparing with the multi-model results from 20 available models that participated in the Scenario Model Intercomparison Project (ScenarioMIP; Table S1 in Supporting Information S1). The above multi-model ensemble simulations were derived from the SSP2-4.5 scenario experiment (using the same model settings as the CLIM_All_ssp2-4.5; O'Neill et al., 2016). All multi-model outputs were interpolated onto a common grid (approximately 2.8° × 2.8°) to facilitate comparison.

Then, the human-driven changes in precipitation until the mid-21st century were examined by comparing the average results of the later 10-year period (2041–2050) under the COVID-MIP emission-reduction conditions with results for the same period from the baseline case.

2.3. Performance of the BCC_AGCM2.0_CUACE/Aero Model in Simulating Precipitation Sensitivity to Anthropogenic Forcings

As shown in Figures S4a and S4b in Supporting Information S1, the simulations from the BCC_AGCM2.0_CUACE/Aero model show comparable spatial and meridional distributions to the multi-model mean results from the SSP2-4.5 scenario experiment. However, the global mean result of boreal summer mean rainfall from the BCC_AGCM2.0_CUACE/Aero simulations is 2.7 mm month^{-1}, which is slightly less than that based on the multi-model simulations (3.1 mm month^{-1}). The above difference in the global mean results is mainly attributed to the weak peak of precipitation north of the equator from the BCC_AGCM2.0_CUACE/Aero simulations (as shown in the line charts in Figures S4a and S4b in Supporting Information S1). Also, the BCC_AGCM2.0_CUACE/Aero model tends to overestimate the precipitation in parts of the West Pacific and northern Indian Ocean regions, whereas underestimating it in northern side of equatorial Africa, northern parts of South America, and the equatorial Atlantic, relative to the multi-model mean result. These regions with large precipitation differences between the BCC_AGCM2.0_CUACE/Aero and the ScenarioMIP models are mainly concentrated at tropics. Previous studies reported that the CMIP6 models show a large spread in the precipitation projections at tropics, particularly over the Afro-Asian monsoon regions consisting of the East Asian, South Asian, and North African monsoon regions (Chen et al., 2022). Figure S4c in Supporting Information S1 shows the global and meridional distributions of inter-model standard deviation of the projected precipitation based on the ensemble simulations of 20 ScenarioMIP models, which present the peak of zonal mean standard deviation at the NH tropics. The values of inter-model standard deviation are apparent large over northern side of equatorial Africa, Asian monsoon regions, and eastern parts of equatorial Pacific and Atlantic, with the signal-to-noise ratio less than 1.5 at the adjacent areas. These results indicate inherent differences among the precipitation projections of the ScenarioMIP models in the aforementioned regions. The uncertainty of the above precipitation projections could arise from the model-dependent responses of circulation to anthropogenic forcings (Chen et al., 2020). Limited horizontal resolution makes it challenging for most ScenarioMIP models to properly resolve the complex topographies over the coastal regions of continents, as well as the Maritime Continent, which also contribute to the uncertainty of projected precipitation changes over these areas (Liang et al., 2022). The preceding analyses partly explain the precipitation differences at tropics between the BCC_AGCM2.0_CUACE/Aero and the ScenarioMIP models (Figures S4a and S4b in Supporting Information S1).

The results from the BCC_AGCM2.0_CUACE/Aero model show comparable temporal trends to the multi-model simulations from the SSP2-4.5 scenario experiment before the 2040s, while the former present a larger increase in precipitation in the 2040s than the latter (Figure S5 in Supporting Information S1). This difference in trend could be attributed to the greater precipitation sensitivity by the BCC_AGCM2.0_CUACE/Aero model to decreased aerosol emissions under the baseline scenario. One possible reason for this is a small value of lower bounds for cloud droplet number concentration (CDNC) prescribed by the BCC_AGCM2.0_CUACE/Aero model, which leads to a large absolute value of aerosol indirect effects (Hoose et al., 2009; H. Zhang et al., 2016). Additionally, the value calculated by the BCC_AGCM2.0_CUACE/Aero model for the climate sensitivity parameter α, defined as the reciprocal of the climate feedback parameter, is $-1.50°C$ (W m^{-2})$^{-1}$, which is greater in magnitude than the best estimated value of $-0.862°C$ (W m^{-2})$^{-1}$ given by IPCC AR6, but within the very likely range of -1.961 to $-0.552°C$ (W m^{-2})$^{-1}$ (Forster et al., 2021; H. Zhang et al., 2022). This slightly large value of α may lead to the relatively strong responses of warming and the resulting precipitation to reductions in aerosol emissions in the mid-21st century under the SSP2-4.5 scenario (Allan et al., 2010; Fiedler et al., 2019; Lund et al., 2019; Westervelt et al., 2015). Overall, our results are generally consistent with the precipitation projections for the first half of the 21st century under the SSP2-4.5 scenario from the ScenarioMIP ensemble simulations.

3. Results

3.1. Responses of Boreal Summer Mean Precipitation to Reductions of Various Anthropogenic Forcings

Under the COVID-MIP green economic-recovery scenarios, the differences in boreal summer mean rainfall between the 2020s and 2040s feature general increases in the Northern Hemisphere (NH), except for western

Europe and parts of North America, but apparent decreases at low latitudes of the Southern Hemisphere (SH), particularly over southeastern Indian Ocean and southern Pacific (figures not shown). As shown in Figure S1 in Supporting Information S1, WMGHG concentrations, except for CH_4, still slightly increase during the period 2020–2050 under the MGR and SGR scenarios, even though emissions of these WMGHGs decrease significantly relative to the baseline case (Forster et al., 2020). The actual changes in precipitation in the 2040s relative to the 2020s under these scenarios are still driven by increased WMGHG and aerosol reductions (Figures S1 and S2 in Supporting Information S1), which explains that the above rainfall responses are partially similar to the results noted in previous studies that focused on widely used global warming scenarios (e.g., representative concentration pathway or SSP scenarios; Geng et al., 2020; Kang, 2020; Tan et al., 2008). This implies that WMGHG emissions mitigation until the mid-21st century may not reverse the precipitation changes caused by global warming. It is still necessary to promote more aggressive WMGHGs emission mitigation measures in the future to alleviate the regional wetting or drying driven by WMGHGs (He et al., 2020; B. Wang et al., 2020). Therefore, in this study, we primarily focused on the precipitation changes in the 2040s under the COVID-MIP green economic-recovery scenarios relative to the baseline case at the same period, and investigated the combined and individual contributions of reductions in various anthropogenic forcing agents.

Among different forcings, reducing aerosols plays an opposite role to decreasing WMGHG emissions in terms of precipitation changes relative to the baseline case in the 2040s, particularly at the NH middle and high latitudes, the north-equatorial parts of eastern Pacific and Atlantic, the Indian Ocean, and the middle latitudes of the SH (Figures 1c–1f). The decreased aerosols contribute to great global mean rainfall increase of 1.7 [1.6 to 1.9] (1.2 [1.0 to 1.3]) mm month^{-1} under the SGR (MGR) scenario relative to the baseline case, while the reduction in WMGHG emissions results in decreases in global mean rainfall by −0.8 [−1.0 to −0.6] and −0.9 [−1.1 to −0.7] mm month^{-1} under the MGR and SGR scenarios, respectively (Figures 2a–2c). Compared to the baseline case in the 2040s, the increases in boreal summer mean rainfall in CLIM_All are striking in the NH (except for western and central Eurasia), while the opposite changes in rainfall appear mainly in Southeast Asia, southern Pacific, and South America (Figures 1a and 1b). As a result, the spatial distributions of the above precipitation changes are apparently asymmetrical between the two hemispheres. This study further calculated the interhemispheric contrast of boreal summer mean rainfall under different scenarios for the CLIM_All, CLIM_Aero, and CLIM_GHG groups, respectively. In the 2040s, the interhemispheric differences in precipitation in CLIM_All are increased by 2.2 [0.6 to 3.7] and 3.2 [2.2 to 4.3] mm month^{-1} under the MGR and SGR scenarios, respectively, compared to the baseline case, which are larger in magnitude than the changes in CLIM_Aero and CLIM_GHG (Figure 2d).

The zonal-mean results show that the above increased interhemispheric contrast in rainfall under the COVID-MIP green economic-recovery scenarios in CLIM_All could be attributable to the opposite changes in precipitation at low latitudes between the two hemispheres due to anthropogenic emissions mitigation (Figure 3). Among different experiments, the meridional changes in zonal-mean precipitation in CLIM_All are similar to the corresponding changes in CLIM_Aero in the NH and at low latitudes of the SH (black and bright green lines in Figure 3). This indicates that variation on aerosols dominates the changes in boreal summer mean rainfall at the above latitudes, contributing to an asymmetric response of tropical precipitation bounded by the equator (Allen, 2015). Conversely, decreasing WMGHG emissions results in decreases in zonal-mean precipitation at most of latitudes, particularly at the middle latitudes of the SH (dark green lines in Figure 3). This decrease counteracts the effect of reduction of aerosols on precipitation at the SH middle latitudes, leading to negligible changes in rainfall in CLIM_All at these latitudes. Ultimately, the combined effect of simultaneous reductions in WMGHG and aerosol emissions enhances the asymmetric response of precipitation between the two hemispheres in the 2040s.

3.2. Anomalous Atmospheric Circulation Associated With Reductions in Various Anthropogenic Forcings

The underlying mechanism causing the rainfall changes described above is explored by examining atmospheric circulation and water vapor anomalies driven by reductions in anthropogenic forcings under the COVID-MIP green economic-recovery scenarios (Figures 4 and 5). Compared to the baseline case in the 2040s, negative sea level pressure (SLP) anomalies are generally found over southern parts of Eurasia in CLIM_All and CLIM_Aero (Figures 4a–4d). In CLIM_All, positive SLP anomalies appear mainly over South Africa, Oceania, southeastern Pacific, and southern Atlantic, while such anomalies are striking over the tropical Pacific, Atlantic, and the
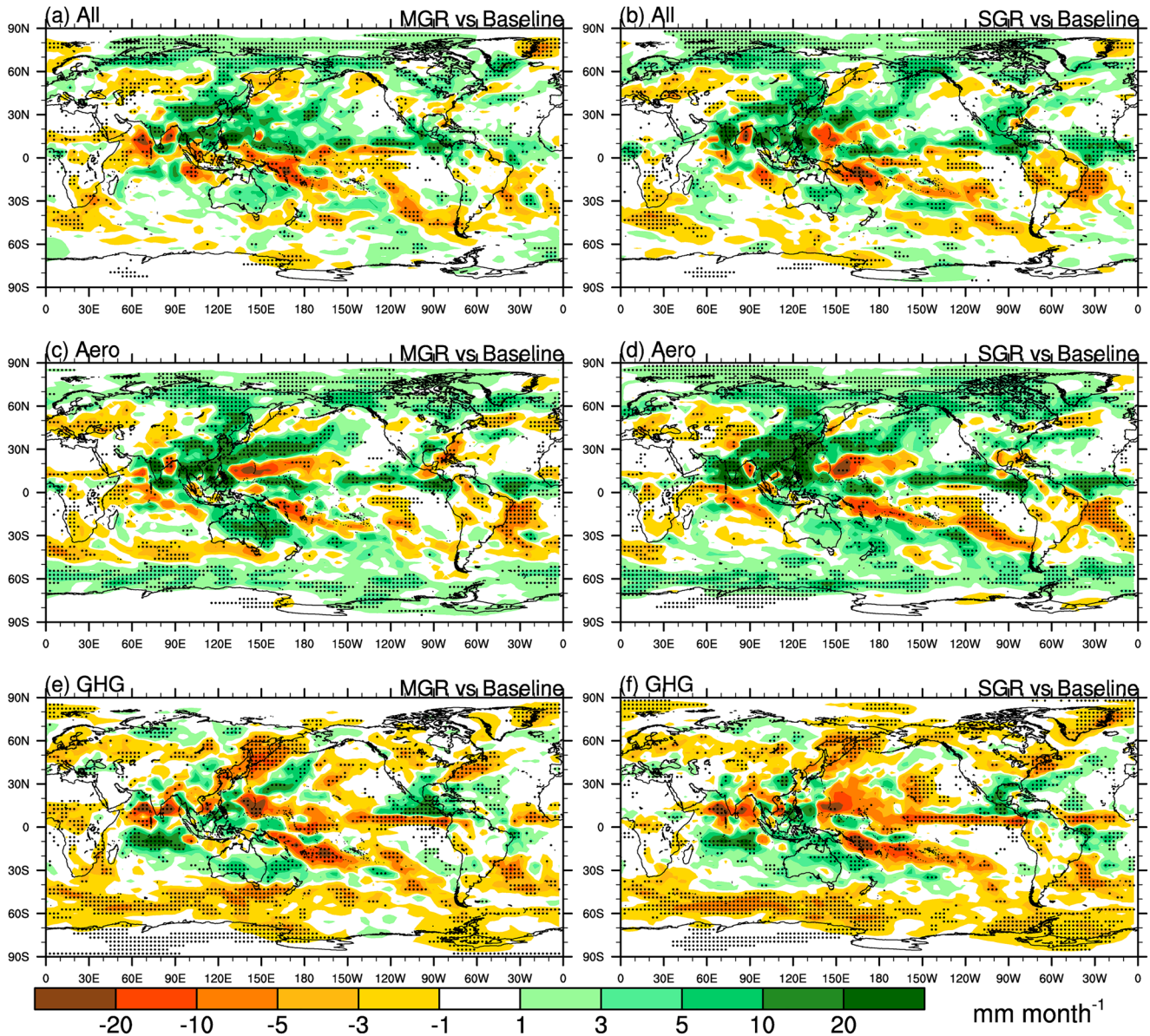
Figure 1. Spatial distribution of changes in boreal summer mean precipitation (unit: mm month^{-1}) in the 2040s (2041–2050) under the (a, c, and e) moderate green economic-recovery (MGR) and (b, d, and f) strong green economic-recovery (SGR) scenarios relative to the baseline case at the same period for the (a, b) CLIM_All, (c, d) CLIM_Aero, and (e, f) CLIM_GHG groups. Dots indicate statistically significant differences at the ≥90% confidence level via the two-tailed Student's t-test.

middle latitudes of the SH in CLIM_Aero. These SLP anomalies are consistent with a series of cyclonic anomalies along the south and east coasts of Eurasia at 850 hPa, which enhance the seasonal prevailing winds that transport atmospheric water vapor from western Pacific and northern Indian Ocean to Inner Eurasia, and induce water vapor convergence anomalies over the Asia summer monsoon region (Figures 5a–5d). This anomalous atmospheric circulation may be primarily attributable to the enhanced land-ocean thermal contrast, characterized by greater warming over Eurasia than the surrounding oceans (Figures S6a–S6d in Supporting Information S1), due to decreased aerosol emissions and the resulting positive radiative forcing in their source areas (Figures S3b, S3c, S3e, and S3f in Supporting Information S1; Z. Wang et al., 2015; A. D. Zhao et al., 2018). Striking reduction in aerosols in southern and eastern parts of Eurasia results in stronger surface warming and atmospheric heating in the NH than that in the SH (Figures S6a–S6d, S7a, S7b, S7d, and S7e in Supporting Information S1), leading to anomalous ascending flow and negative SLP anomalies over southern Eurasia and its surrounding oceans (Figures 4a–4d; Yang et al., 2022). In contrast, anomalous subsidence can be found in the mid-to-low latitudes in
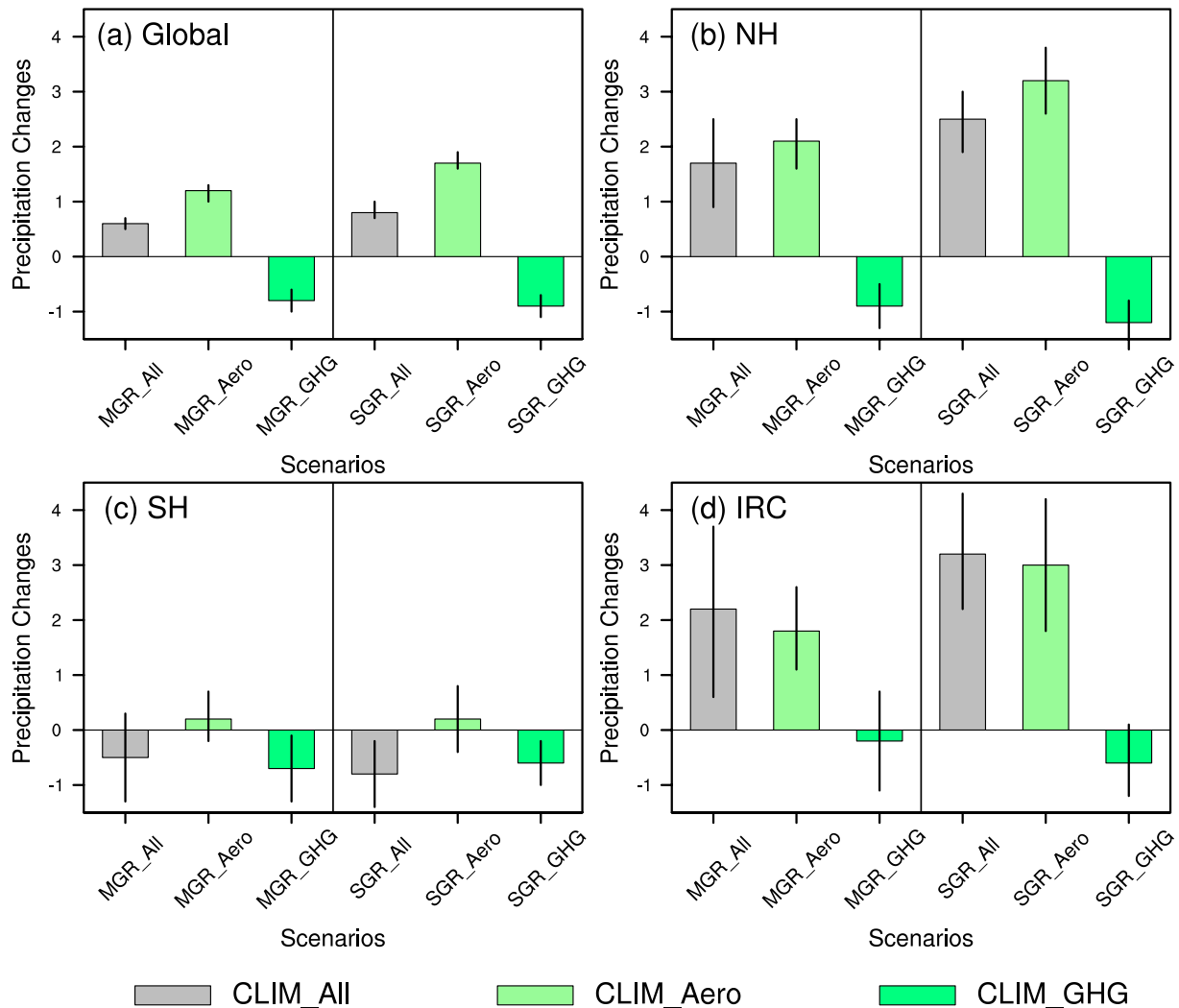
Figure 2. Under different scenarios, (a) Global mean, (b) North Hemispheric mean, and (c) South Hemispheric mean changes in boreal summer mean precipitation (unit: mm month^{-1}) in the 2040s relative to the baseline case at the same period. (d) Changes in interhemispheric rainfall contrast (IRC; unit: mm month^{-1}; differences in regional mean results between the NH and SH precipitation; Positive values represent larger increases in boreal summer rainfall in the NH than those in the SH) in the 2040s under different scenarios relative to the baseline case at the same period. The gray, bright green, and dark green bars represent the results based on the CLIM_All, CLIM_Aero, and CLIM_GHG group, respectively. The line on each bar indicates the 5%–95% confidence interval for precipitation changes.

the SH in CLIM_All and CLIM_Aero (Figures S7a, S7b, S7d, and S7e in Supporting Information S1), inducing positive SLP anomalies in this region (Figures 4a–4d; H. Wang et al., 2019). As a result, the above SLP anomalies reinforce the climatological SLP gradient, conducive to cross-equatorial flow to transport lower-troposphere moisture to the NH (Westervelt et al., 2015; Wilcox et al., 2020; A. D. Zhao et al., 2018).

Compared to the baseline case, reducing WMGHG emissions plays an opposite role to decreasing aerosols in terms of atmospheric circulation changes, particularly at the middle latitudes over eastern Eurasia and the surrounding oceans (Figures 4e and 4f). In CLIM_GHG, positive SLP anomalies are found over eastern Asia, accompanied by several anticyclonic anomalies at 850 hPa over the same area. These SLP anomalies are attributable to strong atmospheric cooling driven by decreased WMGHGs that produces anomalous descending
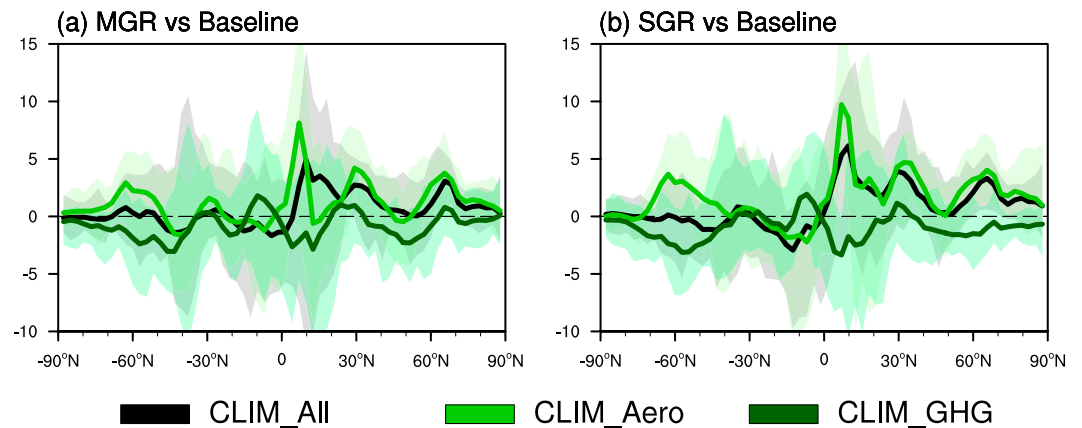
Figure 3. Meridional distribution of zonal mean changes in boreal summer mean precipitation (unit: mm month^{-1}) in the 2040s under the (a) moderate green economic-recovery (MGR) and (b) strong green economic-recovery (SGR) scenarios relative to the baseline case at the same period. The black, bright green, and dark green lines represent the results based on the CLIM_All, CLIM_Aero, and CLIM_GHG group, respectively. The shadings represent the spread of 10 ensemble members, while the solid lines show the multi-member mean results.

motion in the middle and lower troposphere near 50°N (Figures S7c and S7f in Supporting Information S1; Wei et al., 2022; Yang et al., 2022). In addition, negative SLP and anticyclonic anomalies are apparent over southern Indian Ocean, parts of Oceania, and southwestern Pacific, while the opposite changes appear mainly near 60°S (Figures 4e and 4f). These SLP anomalies are also consistent with the meridional circulation changes featured with anomalous ascending (descending) motion south of the equator (north of 60°S) (Figures S7c and S7f in Supporting Information S1). The above atmospheric circulation anomalies enhance equatorward water vapor transport in both hemispheres and induce water vapor convergence anomalies over southern Indian Ocean and southwestern Pacific (Figures 5e and 5f), ultimately contributing to decreased interhemispheric contrast of boreal summer rainfall (Figure 2d).

Moreover, vigorous atmospheric convective activities also contribute to the development of precipitation at local scale (Lau & Kim, 2017). Compared to the baseline case, strong negative vertical velocity anomalies, that is, anomalous ascents, are present at 500 hPa over southern Eurasia, parts of northwestern Pacific, and Oceania, in CLIM_Aero (Figures S8c and S8d Supporting Information S1). These enhanced atmospheric convective activities are conducive to the increases in precipitation in these areas (Figures 1c and 1d). Conversely, marked positive vertical velocity anomalies, that is, anomalous descents, are found at 500 hPa over eastern and central Pacific in CLIM_GHG (Figures S8e and S8f in Supporting Information S1), leading to general decreases in precipitation in those areas (Figures 1e and 1f). The changes in vertical velocity described above are opposite to those over southern Indian Ocean. The zonal dipole structure in vertical velocity pattern at 500 hPa over the tropical Pacific and Indian Ocean is coincident with the WMGHG-driven surface air temperature (SAT) anomalies featuring strong cooling over the eastern Pacific and relative weak cooling over the southern Indian Ocean (Figures S6e and S6f in Supporting Information S1). The above patterns of vertical velocity and SAT anomalies indicate that decreasing WMGHG emissions may modify boreal summer rainfall by enhancing the east-west asymmetry of SAT anomalies and the resulting Walker circulation anomalies (DiNezio et al., 2013; Lau & Kim, 2015, 2017), leading to increases (decreases) in precipitation over the southern Indian Ocean (eastern Pacific). The SAT response in the tropics to WMGHG forcing is similar but opposite in sign to that response noted by B. Wang et al. (2020), which implies that the La Niña-like eastern Pacific cooling may emerge due to the decreasing WMGHG emissions, causing to increased boreal summer rainfall over large areas of the North American monsoon region (Figures 1e and 1f, Figures S6e and S6f in Supporting Information S1).

Compared to the baseline case, apparent positive vertical velocity anomalies appear at 500 hPa along eastern Indian Ocean, the south-equatorial parts of the Pacific, and northern South America in CLIM_All, while negative anomalies of vertical velocity are generally present on the other side of the equator (Figures S8a and S8b in Supporting Information S1). Such "northern ascent and southern descent" patterns of vertical velocity anomalies bounded by the equator support prominent zonal-mean water vapor convergence (divergence) anomalies north (south) of the equator (black lines in Figure S9 in Supporting Information S1), indicating potential contributions
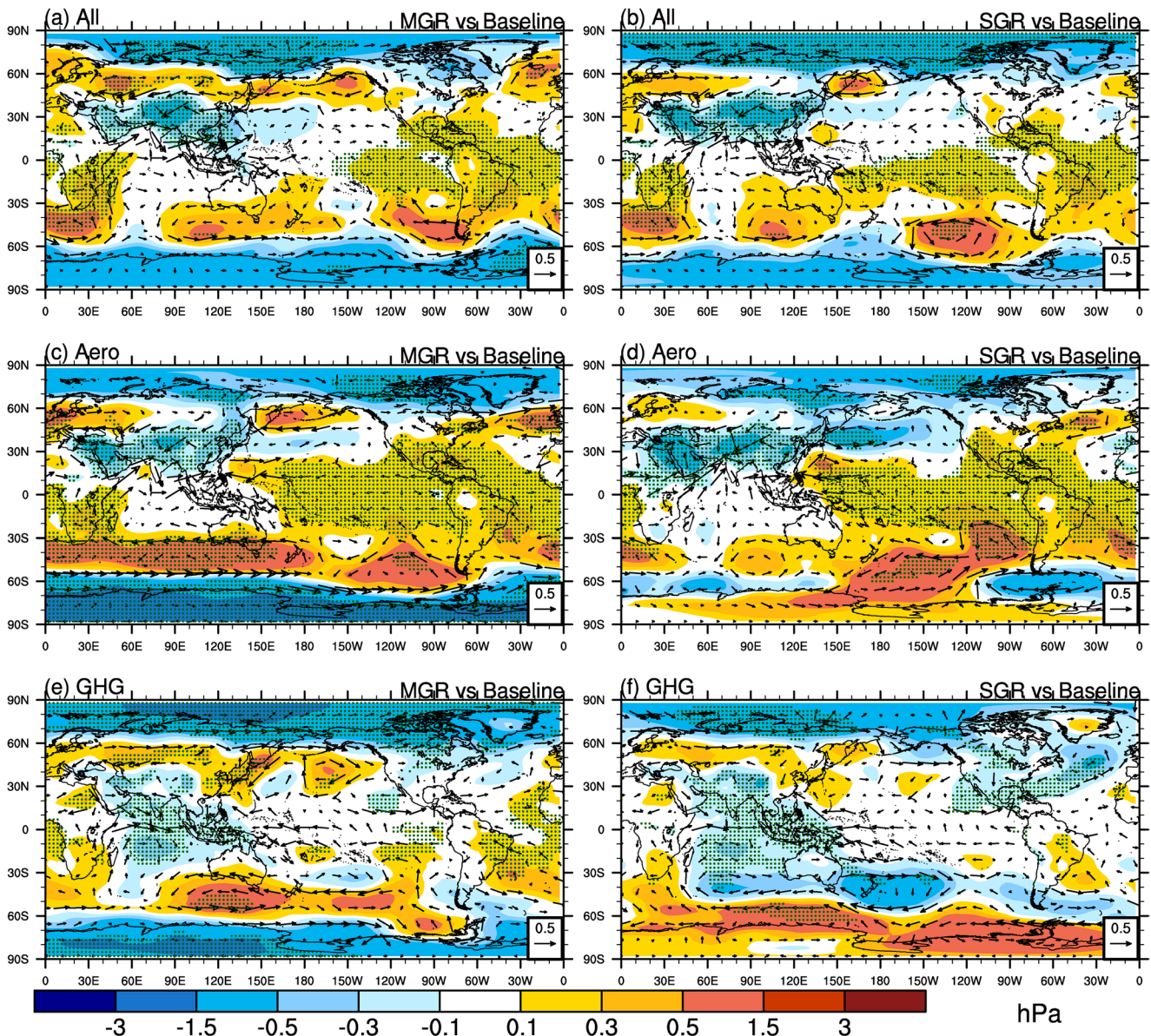
Figure 4. Changes in boreal summer mean sea level pressure (color, unit: hPa) and wind (vector, unit: m s^{-1}) at 850 hPa in the 2040s under the (a, c, and e) moderate green economic-recovery (MGR) and (b, d, and f) strong green economic-recovery (SGR) scenarios relative to the baseline case at the same period for the (a, b) CLIM_All, (c, d) CLIM_Aero, and (e, f) CLIM_GHG groups. Dots indicate statistically significant differences at the ≥90% confidence level via the two-tailed Student's t-test.

to boreal summer rainfall from anthropogenically driven thermodynamic and dynamic structure changes in the deep tropics (Allen, 2015; H. Wang et al., 2020; Z. Wang et al., 2015). Therefore, the corresponding responses to the decreased WMGHG and aerosol emissions from meridional atmospheric circulation are investigated in next section.

3.3. Responses of Meridional Overturning Circulation in the Tropics to Reductions in Various Anthropogenic Forcings

By analyzing the results from various forcing experiments based on the COVID-MIP green economic-recovery scenarios, this study presented an increased interhemispheric contrast of boreal summer mean rainfall in CLIM_All compared to the baseline case in the 2040s, which is attributable to general increases in rainfall in the NH but opposite changes at low latitudes of the SH (Figure 3). Considering the meridional dipole structure in this anomalous rainfall pattern at low latitudes between the two hemispheres and the dramatic water vapor convergence
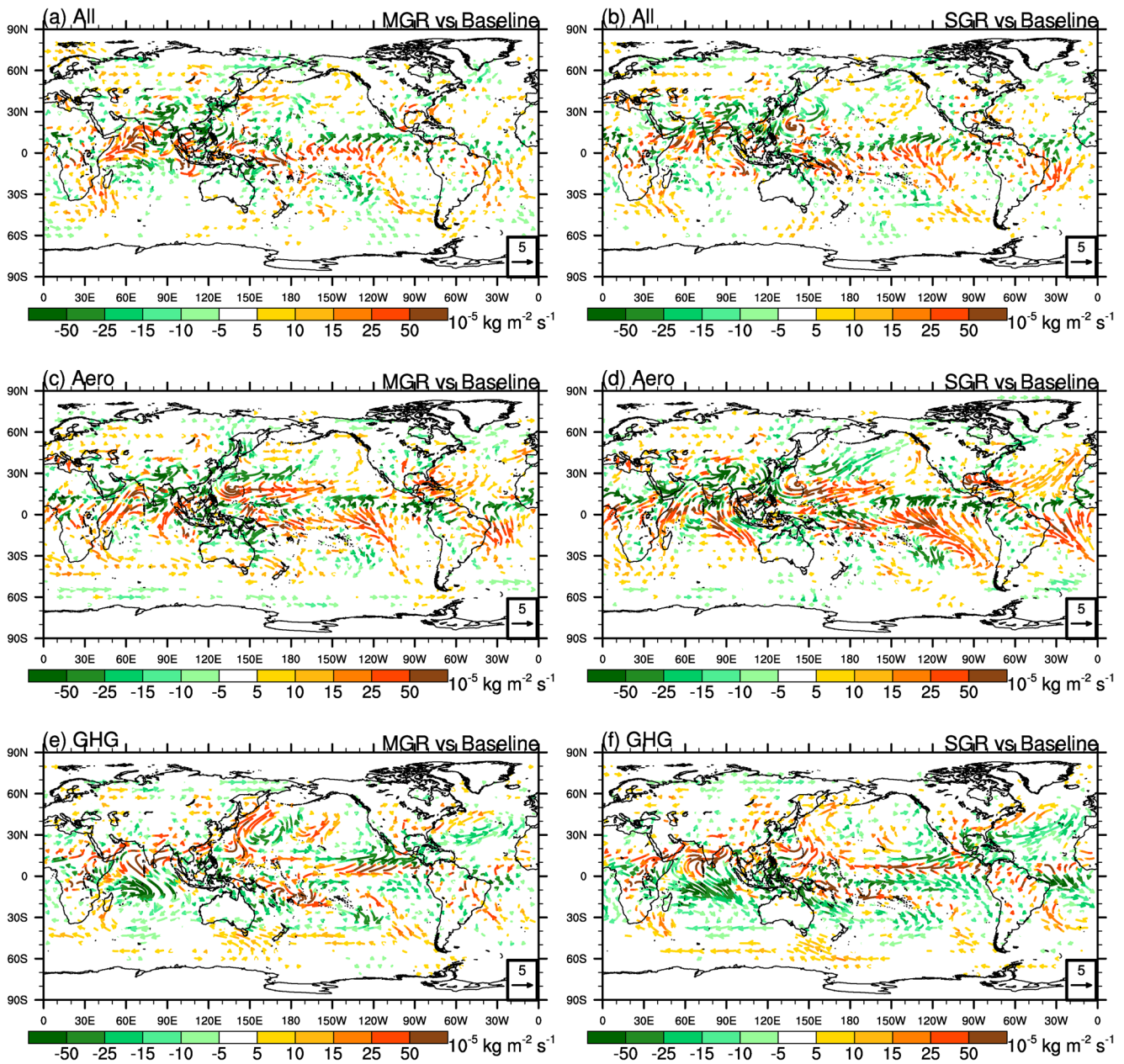
Figure 5. Changes in boreal summer mean water vapor transport (vector, unit: 10^2 kg m^{-1} s^{-1}) and divergence (color, unit: 10^{-5} kg m^{-2} s^{-1}) in the middle to lower troposphere in the 2040s under the (a, c, and e) moderate green economic-recovery (MGR) and (b, d, and f) strong green economic-recovery (SGR) scenarios relative to the baseline case at the same period for the (a, b) CLIM_All, (c, d) CLIM_Aero, and (e, f) CLIM_GHG groups.

(divergence) anomalies north (south) of the equator (black lines in Figure S9 in Supporting Information S1), detailed analysis for changes in meridional overturning circulation in the tropics in response to decreased WMGHG and aerosol emissions is provided in this section. This would help to explore the underlying mechanisms by which various forcings modify precipitation distributions from the perspective of the cross-equatorial asymmetry in energy budget and the resulting anomalous Hadley circulation (Allen, 2015; H. Wang et al., 2020).

Zonal mean changes in boreal summer mean meridional streamfunction (MS) are shown in Figure 6 to illuminate the effects of decreased WMGHG and aerosol emissions individually or simultaneously on the Hadley cell. In boreal summer, the Hadley cell features anticlockwise meridional circulation (the dashed contours in Figure 6), accompanied by upward (downward) motions north (south) of the equator and northward cross-equatorial flows in the lower troposphere (H. Wang et al., 2020). Negative MS anomalies in the tropics represent anticlockwise
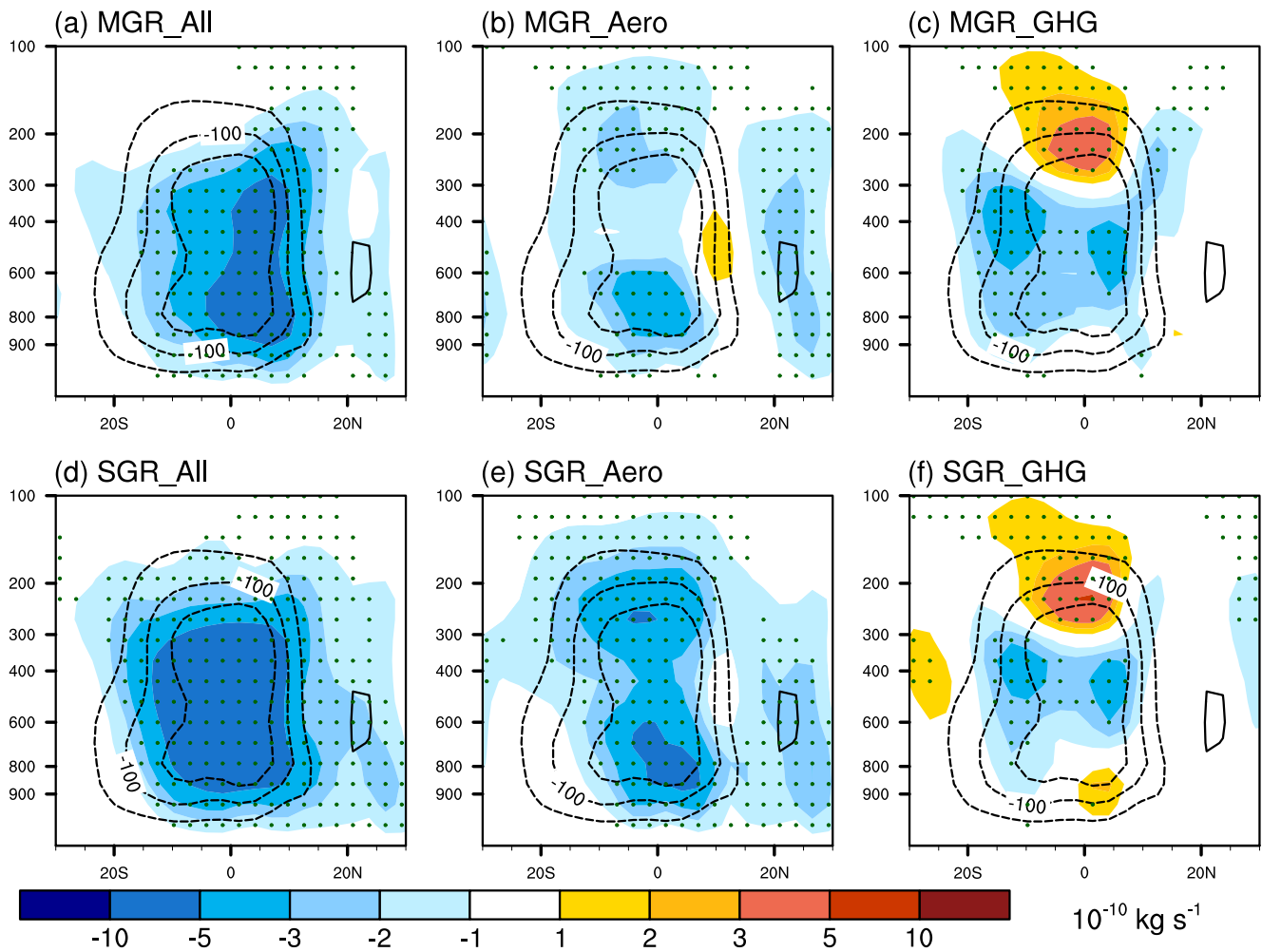
Figure 6. Zonal mean changes in boreal summer mean meridional streamfunction (unit: 10^{-10} kg s^{-1}) in the 2040s under the (a–c) moderate green economic-recovery (MGR) and (d–f) strong green economic-recovery (SGR) scenarios relative to the baseline case for the (a, d) CLIM_All, (b, e) CLIM_Aero, and (c, f) CLIM_GHG groups. Contours denote the climatology (the 2020–2050 mean results from the baseline case), while colors represent changes under the COVID-MIP green economic-recovery scenarios relative to the baseline case. Negative values of both contours and colors indicate anticlockwise circulation. Dots indicate statistically significant differences at the ≥90% confidence level via the two-tailed Student's t-test.

meridional circulation patterns, which strengthen the climatological Hadley cell and thereby contribute to northward moisture transport in the lower troposphere. Compared to the baseline case in the 2040s, notable negative MS anomalies are found throughout the troposphere in the tropics in CLIM_All and CLIM_Aero (Figures 6a, 6b, 6d, and 6e). These anomalous anticlockwise meridional circulation patterns explain the enhanced northward moisture transport in the lower troposphere at tropics (Figures 5a–5d), ultimately contributing to increases of intertropical rainfall contrast bounded by the equator (Figure 7a). In CLIM_All and CLIM_Aero, atmospheric aerosol contents decrease apparently at their source areas, that is, the NH (Figures S3b, S3c, S3e, and S3f in Supporting Information S1), under the COVID-MIP green economic-recovery scenarios relative to the baseline case, leading to larger warming in the NH than that in the SH (Figures S6a–S6d, S7a, S7b, S7d, and S7e in Supporting Information S1). These increases of interhemispheric temperature contrast result in enhanced Hadley cell to balance the interhemispheric asymmetry in energy budget (Figures 6a, 6b, 6d, and 6e), which transports energy away from the NH to the SH via the upper branches, whereas delivering moisture from the SH to the NH by the lower branches as compensation (Allen et al., 2015; Chiang & Friedman, 2012; Frierson & Hwang, 2012). The atmospheric cross-equatorial heat transport is also calculated, which is the key ingredient of the theoretical framework introduced by Kang et al. (2008, 2009) to interpret the ITCZ migration as a response to extratropical forcing alone (Frierson & Hwang, 2012). Compared to the baseline case, atmospheric cross-equatorial heat transport decreases in CLIM_All and CLIM_Aero (Figure 7b), representing increased heat transport to the SH,
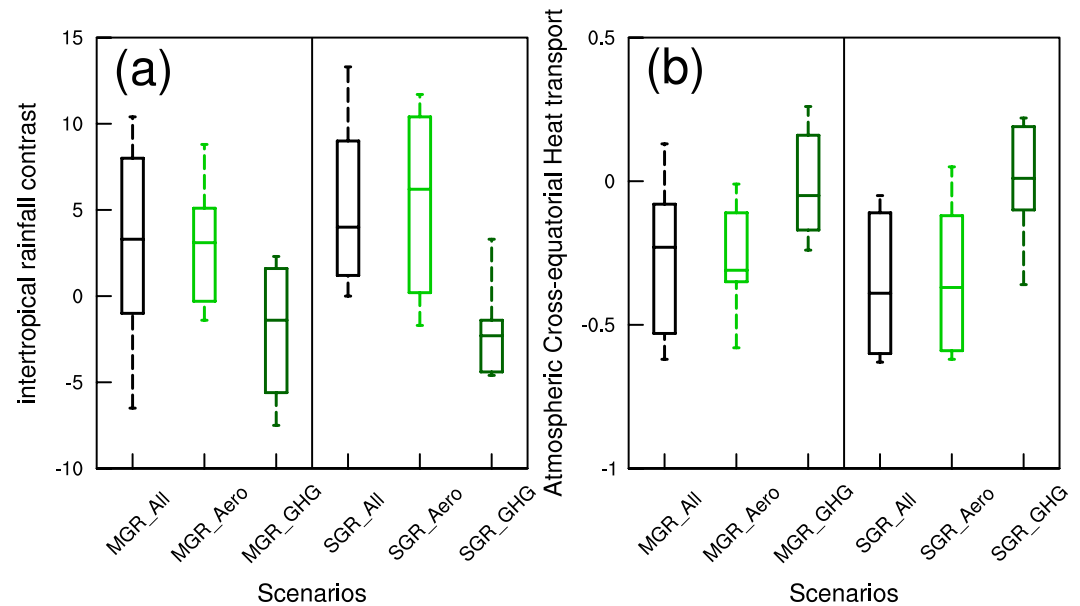
Figure 7. Changes in (a) intertropical contrast of boreal summer mean rainfall (differences in regional mean results between the NH tropical [0–20°N, 0–360°] and SH tropical [0–20°S, 0–360°] precipitation; unit: mm month^{-1}) and (b) atmospheric cross-equatorial heat transport (unit: PW) in the 2040s under different scenarios compared to the baseline case. Positive values in (a) represent larger increases in precipitation in the NH tropics than those in the SH tropics, while negative values in (b) represent enhanced southward transport of atmospheric cross-equatorial heat under the COVID-MIP green economic-recovery scenarios, relative to the baseline case. Each box-and-whisker plot shows the spread of the 25th to the 75th percentile of 10 ensemble members (lower and upper borders of the box, respectively), the median (the center line of the box), as well as extreme values (endpoints of the whiskers). The black, bright green, and dark green lines represent the results based on the CLIM_All, CLIM_Aero, and CLIM_GHG group, respectively.

which is consistent with the enhanced Hadley cell and contributes to increases in precipitation in a warmer NH (Allen, 2015; Z. Wang et al., 2015; A. D. Zhao et al., 2018).

Conversely, positive MS anomalies appear in the upper troposphere over the equator and in the lower troposphere north of the equator in CLIM_GHG relative to the baseline case (Figures 6c and 6f), weakening the climatological Hadley cell and thereby contributing to anomalous moisture convergence in the lower troposphere over the low latitudes of the SH (dark green lines in Figure S9 in Supporting Information S1). These meridional circulation anomalies are partially attributable to the decreases of interhemispheric temperature contrast (stronger negative SAT anomalies over the NH continents than those over the SH oceans) due to reduction of WMGHG emissions (Figures S6e, S6f, S7c, and S7f in Supporting Information S1), weakening the southward transportation of energy by the upper branches of the Hadley cell (Figure 7b). Note that this study investigates the response of interhemispheric thermal contrast (ITC) to anthropogenic emissions mitigation by referring to the differences in regional mean results of SAT between two key areas, that is, the NH continents (20–50°N, 0–360°) and the SH oceans (20–50°S, 0–360°). This approach helps to avoid the disturbance of the polar SAT since the CMIP simulations show large uncertainty in temperature in polar regions (Bracegirdle et al., 2020; Xu et al., 2013). In addition, strong cooling centers driven by decreased WMGHGs are apparent in the middle and lower troposphere in the mid-to-high latitudes in both hemispheres and in the upper troposphere in the tropics (Figures S7c and S7f in Supporting Information S1). These thermal structure changes weaken (enhance) the zonal wind in the upper troposphere at the equator (in the middle and lower troposphere near 30°S and 60°N) through the thermal wind balance (Figures S10c and S10f in Supporting Information S1; H. Wang et al., 2016), leading to clockwise meridional circulation anomalies, that is, positive MS anomalies over the equator (Figures 6c and 6f). The above meridional circulation changes weaken the climatological Hadley cell and thereby suppress the northward transport of lower-troposphere moisture. As a result, striking tropical precipitation increases appear south of the equator in CLIM_GHG, compared to the baseline case, whereas the opposite changes are present on the other side of the equator (Figure 7a). These WMGHG-driven changes in the ITC and precipitation are similar but opposite in sign to the responses noted by previous studies focused on widely used global warming scenarios (B. Wang

et al., 2020; Chou et al., 2007; Lau & Kim, 2017; Tan et al., 2008), which contribute to decreases of interhemispheric rainfall contrast (IRC) in CLIM_GHG relative to the baseline case (Figure 2d).

4. Discussion

Previous studies reported a slight increase of 0.2% in global greenhouse gases emissions for 2021 compared to the 2019 levels, without considering land-use, land change, and forestry (Crippa et al., 2022; Friedlingstein et al., 2022). This suggests that total global greenhouse gases emissions in 2021 will be similar to or even break the record 2019 levels, thereby confirming that reduction in global emissions due to the COVID-19 pandemic is unprecedented but short-lived (United Nations Environment Programme, 2022). However, countries around world still need to make efforts to slow down global warming by reducing greenhouse gases emission to bridge the 2030 emission gap (Sanderson et al., 2016; United Nations Environment Programme, 2022). This motivates the updated scenarios, that is, the COVID-MIP green economic-recovery scenarios, which considered the impact of accelerating decarbonization on socioeconomic development in the 21st century, and thereby obtained the corresponding anthropogenic emission pathways. These green economic-recovery scenarios supplemented the current projections of anthropogenic emission pathways based on the integrated assessment models (Lamboll et al., 2021), and can be regarded as an important tool for identifying possible climate risks within the context of achieving carbon neutrality. Exploration of the subsequent climate responses associated with the COVID-MIP green economic-recovery scenarios is ongoing (D'Souza et al., 2021; J. He et al., 2022; Lei et al., 2022, 2023).

Although two COVID-MIP green economic-recovery scenarios employ lower WMGHG emissions compared to the baseline case, the effective radiative forcing (ERF) of WMGHG increases persistently and may lead to enhanced regional rainfall in a warming world compared to the pre-industrial times (Wentz et al., 2007; Yu et al., 2022). Under this background, the responses of boreal summer rainfall in the mid-21st century to reductions in anthropogenic forcing agents are estimated. The contributions of each agent and the underlying physical mechanisms are investigated in this study. Reduction of aerosol emissions generally plays an opposite role to decreasing WMGHG emissions in driving precipitation changes in the mid-21st century at the global and regional scales (Figures 1c–1f and 2a–2c). This opposite effect of aerosols and WHGMGs on boreal summer rainfall has been noted by previous studies based on CMIP historical runs (Lau & Kim, 2017; L. Zhang & Li, 2016). Changes in precipitation and SAT in CLIM_All compared to the baseline case are generally similar in distribution to those in the sum of CLIM_Aero and CLIM_GHG (Figures 1a and 1b, Figures S6a, S6b, and S11 in Supporting Information S1), which means that these two anthropogenic forcings act partially linearly (Lau & Kim, 2017; L. Zhang & Li, 2016). However, the changes in precipitation and SAT on the sum of CLIM_Aero and CLIM_GHG are larger in magnitude than the changes in CLIM_All, particularly for negative precipitation anomalies in the north-equatorial parts of the West Pacific as well as the SH. This difference in magnitude could be attributed to the nonlinear behavior of climate models in response to reductions in both WMGHGs and aerosols emissions (Bollasina et al., 2011; Ming & Ramaswamy, 2009; L. Zhang & Li, 2016), arising from surface albedo feedback, cloud fields, changes in circulation, and aerosol-cloud interactions (Ming & Ramaswamy, 2009; Soden & Held, 2006). As a result, the linearly composite effect of aerosols and WMGHGs described above indicates that reducing aerosol emissions dominates changes in boreal summer rainfall in the NH and the SH tropics, while WMGHGs-driven precipitation decreases appear mainly in the middle latitudes of the SH. Among different forcing experiments, simultaneous reduction in WMGHG and aerosol emissions contributes to the largest interhemispheric asymmetry in precipitation compared to the baseline case (Figure 2d).

To identify the robust responses of boreal summer rainfall to simultaneous reductions in anthropogenic forcings, model outputs obtained from COVID-MIP and ScenarioMIP are used in this study (Table S2 in Supporting Information S1). These multi-model ensemble simulations were derived from three CMIP6 experiments, namely the ssp245-cov-modgreen experiment, the ssp245-cov-strgreen experiment (using identical model settings and anthropogenic forcings as the CLIM_All), and the SSP2-4.5 scenario experiment (a reference set of simulations using the same model list as COVID-MIP; Table S2 in Supporting Information S1), respectively (Lamboll et al., 2021).

We first showed the spread of the COVID-MIP models in simulating the responses of boreal summer rainfall to anthropogenic emission mitigation and the position of the BCC_AGCM2.0_CUACE/Aero model in this spread. As shown in Figure 8a, increases in global mean precipitation based on the BCC_AGCM2.0_CUACE/Aero simulations are apparently larger than those simulated by the COVID-MIP models. This discrepancy between
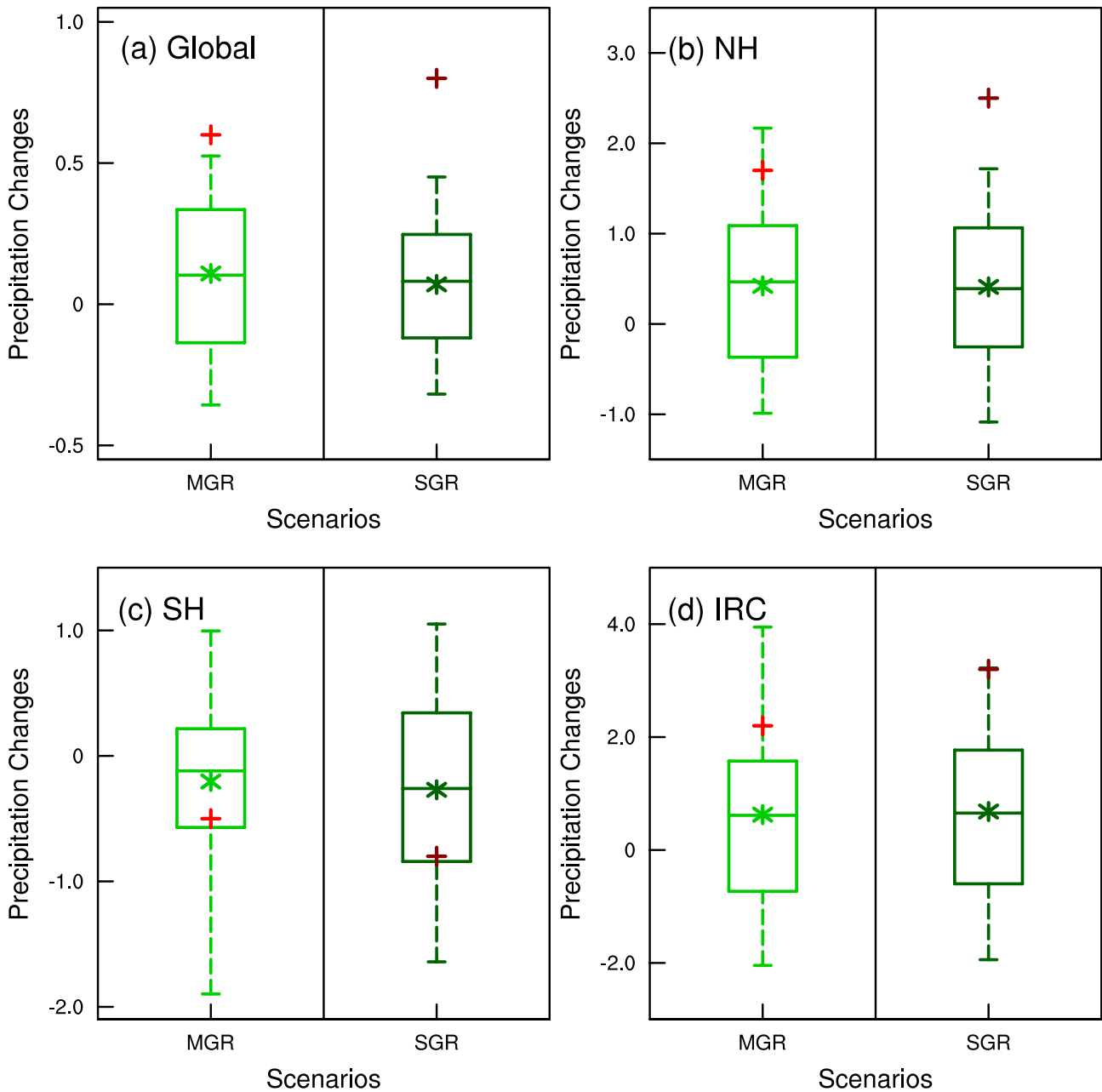
Figure 8. Under different scenarios, (a) Global mean, (b) North Hemispheric mean, and (c) South Hemispheric mean changes in boreal summer mean precipitation (unit: mm month^{-1}) in the 2040s relative to the baseline case at the same period. (d) Changes in the interhemispheric rainfall contrast (IRC) (unit: mm month^{-1}) in the 2040s under different scenarios relative to the baseline case at the same period. Each box-and-whisker plot shows the spread of the 25th and 75th percentiles of 98 ensemble members of six COVID-MIP models (lower and upper borders of the box, respectively), the median (the center line of the box), the 5th and 95th percentiles (lower and upper points of the whiskers, respectively). The bright green and dark green lines represent the multi-model results of the COVID-MIP models corresponding to the moderate green economic-recovery (MGR) and strong green economic-recovery (SGR) scenarios, respectively, while the bright green and dark green asterisks indicate their average values. The red and dark red plus signs represent the mean results based on CLIM_All from the BCC_AGCM2.0_CUACE/Aero simulations.

the BCC_AGCM2.0_CUACE/Aero model and the COVID-MIP ensembles is mainly contributed by the BCC_AGCM2.0_CUACE/Aero simulations showing larger responses of precipitation in the NH to emission reductions (Figure 8b), particularly over the middle and high latitudes (Figures 1a, 1b, and 9). The above differences in rainfall might be attributed primarily to the slab-ocean module incorporated into the BCC_AGCM2.0_CUACE/Aero
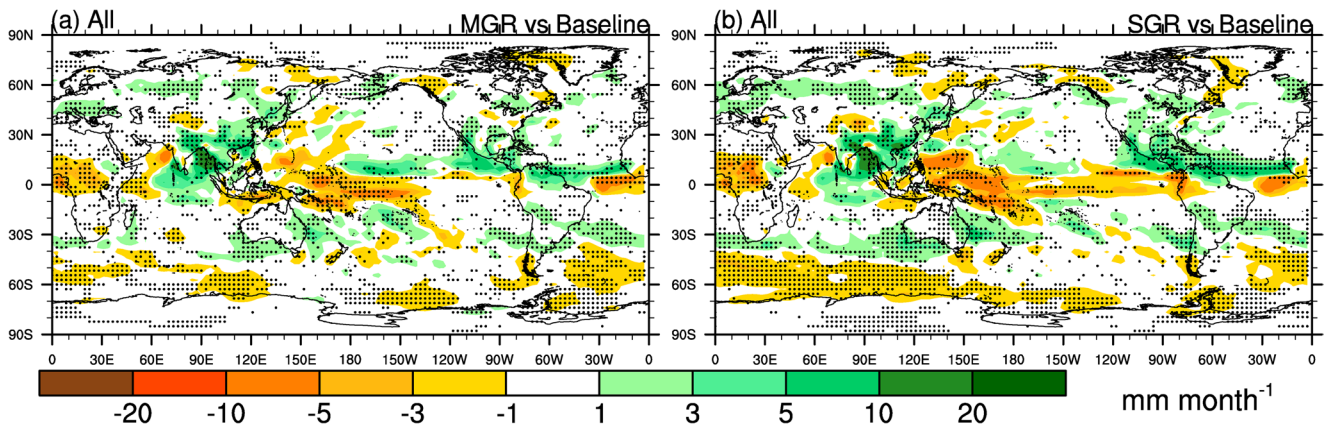
Figure 9. Spatial distribution of changes in boreal summer mean precipitation (unit: mm month⁻¹) in the 2040s under the (a) moderate green economic-recovery (MGR) and (b) strong green economic-recovery (SGR) scenarios relative to the baseline case at the same period. Dots indicate that the differences of more than 80% of ensemble member pairs are same in sign with the averaged difference.

model, which exaggerates responses of the global mean precipitation and the ITCZ migration to anthropogenic forcings via weakening the impact of the ocean on meridional heat transport (Green & Marshall, 2017; Kang, 2020; S. Zhao & Suzuki, 2019). Moreover, as we mentioned in Section 2.3, a small CDNC lower-bound value was set in the BCC_AGCM2.0_CUACE/Aero model, and the climate sensitivity parameter α calculated by this model is relatively large in magnitude (H. Zhang et al., 2016, 2022). These parameters lead to high sensitivity of the BCC_AGCM2.0_CUACE/Aero model to reduction in aerosol emissions (Forster et al., 2021; Hoose et al., 2009), which partially explains the overestimate of our model to increased precipitation in the NH caused by aerosols. Opposing with apparent discrepancy in precipitation responses in the NH between the two types of model simulations, decreases in South Hemispheric mean precipitation based on the BCC_AGCM2.0_CUACE/ Aero simulations are much closer to the multi-model means from the COVID-MIP models (Figure 8c). The former is closer to the lower quartile of the spread of the COVID-MIP simulations.

Currently, there are few models participating in the COVID-MIP (Lei et al., 2022, 2023), of which six available model simulations were adopted in our study (Table S2 in Supporting Information S1). In order to avoid the disturbance of internal variability and inter-model uncertainty on the precipitation response, we obtained as many ensemble members for each model as possible (Deser et al., 2020; Diao et al., 2021; Ourdar et al., 2018), which makes large spread of the COVID-MIP models in simulating precipitation changes and interhemispheric precipitation asymmetricity (Figure 8). Although differences in precipitation changes between the BCC_AGCM2.0_CUACE/Aero and the multi-model simulations are not negligible on regional scales, the changes in precipitation based on the BCC_AGCM2.0_CUACE/Aero simulations generally agree in meridional distribution with those simulated by the COVID-MIP models (Figures 9 and 10). The interhemispheric differences in precipitation based on the BCC_AGCM2.0_CUACE/Aero simulations still fall within the spread of the multi-model results simulated by the COVID-MIP models, above the upper quartile. This indicates that the conclusions drawn in this study based on the BCC_AGCM2.0_CUACE/Aero simulations are reasonable. Overall, both the BCC_AGCM2.0_CUACE/Aero and the COVID-MIP simulations present enhanced IRC until the mid-21st century due to simultaneous reductions in WMGHGs and aerosols emissions. Parts of the NH continents, including southeastern Eurasia and southern North America, may encounter more rainfall in boreal summer under the SGR scenario, compared to the changes under the MGR scenario.

We also investigated the contributors to the magnitude of the IRC using the COVID-MIP simulations. As shown in Figure 11a (Figure 11b), there is a significant positive (negative) correlation between precipitation changes in the NH (SH) and changes in the IRC. This suggests that the amplification of the IRC is closely tied to both the increase of precipitation in the NH and the decrease of precipitation in the SH. The dots based on the BCC_AGCM2.0_CUACE/ Aero simulations fall to the left of the fit lines for the multi-model results from the COVID-MIP models (Figures 11a and 11b). This means that in the BCC_AGCM2.0_CUACE/Aero simulations the increase in precipitation in the NH contributes more to the IRC compared to the decreased precipitation in the SH. The relative leftward position of the BCC_AGCM2.0_CUACE/Aero model results can also be attributed to the high sensitivity of the BCC_AGCM2.0_ CUACE/Aero model to aerosols, as we discussed above, which overestimates increases in precipitation in the NH
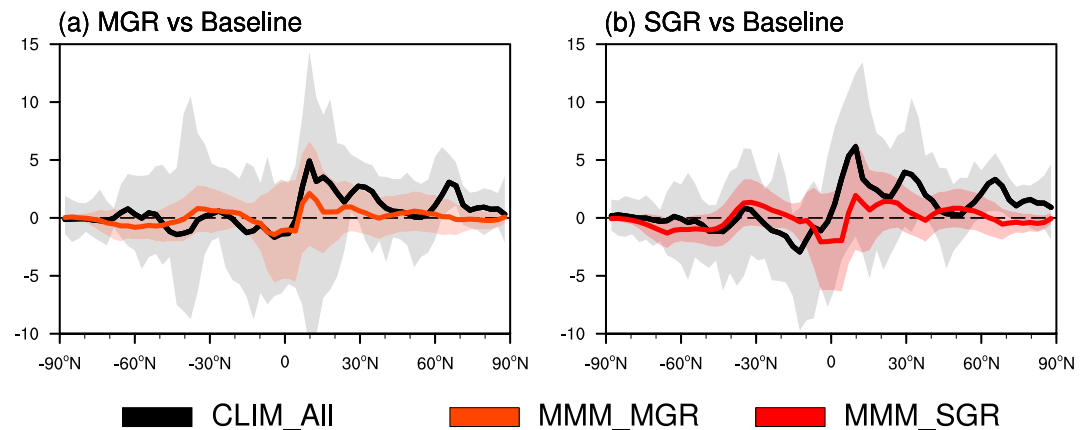
Figure 10. Zonal mean changes in boreal summer mean precipitation (unit: mm month^{-1}) in the 2040s under the (a) moderate green economic-recovery (MGR) and (b) strong green economic-recovery (SGR) scenarios relative to the baseline case at the same period. The black lines represent the results from the BCC_AGCM2.0_CUACE/Aero simulations. The orange and red lines indicate the multi-model means of the COVID-MIP models corresponding to the MGR and SGR scenarios, respectively. The gray (orange and red) shadings represent the spread of 10 ensemble members from the BCC_AGCM2.0_CUACE/Aero simulations (the 5%~95% confidence interval for 98 ensemble members from the COVID-MIP multi-model simulations), while the solid lines represent their average results.

and counteracts the WMGHG-driven decreases in precipitation in the SH (Forster et al., 2021; Hoose et al., 2009; H. Zhang et al., 2016, 2022). In addition, there is a significant positive correlation between changes in the ITC and the corresponding changes in the IRC (Figure 11c). The models that simulate a greater increase in the ITC also tend to yield a larger increase in the IRC, and vice versa, which is similar to the results reported by Chen et al. (2022). Changes in the ITC and IRC from the BCC_AGCM2.0_CUACE/Aero simulations are consistent with the above correlation (Figure 11c). Our study highlights the important role of the ITC in modulating precipitation redistribution, and elucidates mechanism that anthropogenic emission mitigation triggers dynamic responses (e.g., anomalous meridional overturning circulation) through affecting the ITC and then induces interhemispheric precipitation asymmetricity, using sensitivity experiments by the BCC_AGCM2.0_CUACE/Aero model.

Compared to CLIM_Aero, simultaneous-reduced WMGHG and aerosol emissions induces greater losses of precipitation at low latitudes in the SH (Figure 3), which could be attributed primarily to smaller rainfall increase at global scale in CLIM_All (Figure 2a). More importantly, we find significant negative MS anomalies in CLIM_All, larger in magnitude than those in CLIM_Aero, which may indicate strong reinforcing effect of WMGHGs and aerosols, rather than offsetting the impacts of each other, on meridional overturning circulation in the tropics under the conditions of anthropogenic emissions reductions (Figure 6). This stronger Hadley cell also contributes to large decreases in precipitation at the low latitudes of the SH in CLIM_All. In addition, our results present an enhanced interhemispheric asymmetry in rainfall under the SGR scenario than that under the MGR scenario (Figure 2d). This inter-scenario difference in precipitation is consistent with the difference in ERF between two COVID-MIP green economic-recovery scenarios noted by Yu et al. (2022), owing primarily to increases in aerosol-driven climate responses in the NH following stronger emission reductions (Hoose et al., 2009; H. Zhang et al., 2016). The above analyses indicate that climate responses to reduced aerosol emissions take precedence over those to reduction in WMGHG emissions until the mid-21st century under the background of global warming since the industrial era (Westervelt et al., 2015; Wilcox et al., 2020). Since a higher sensitivity of climate responses to the removal of aerosol is found over the major aerosol emission regions, that is, the NH, more aggressive WMGHGs emissions mitigation policies are required to counterbalance the unmasking of the NH warming due to aerosol reduction (Samset et al., 2018; Z. Wang et al., 2015; Westervelt et al., 2015). This may contribute to dampening the NH-SH asymmetry in energy budgets and avoiding regional drying or wetting driven by the subsequent enhanced meridional circulation.

5. Conclusions

Our analysis provides a global-scale preview of how boreal summer precipitation will respond to reduction in anthropogenic emissions in the future by putting two COVID-MIP green economic-recovery scenarios into an aerosol-climate coupled model. We find that simultaneous reductions in WMGHGs and aerosols apparently
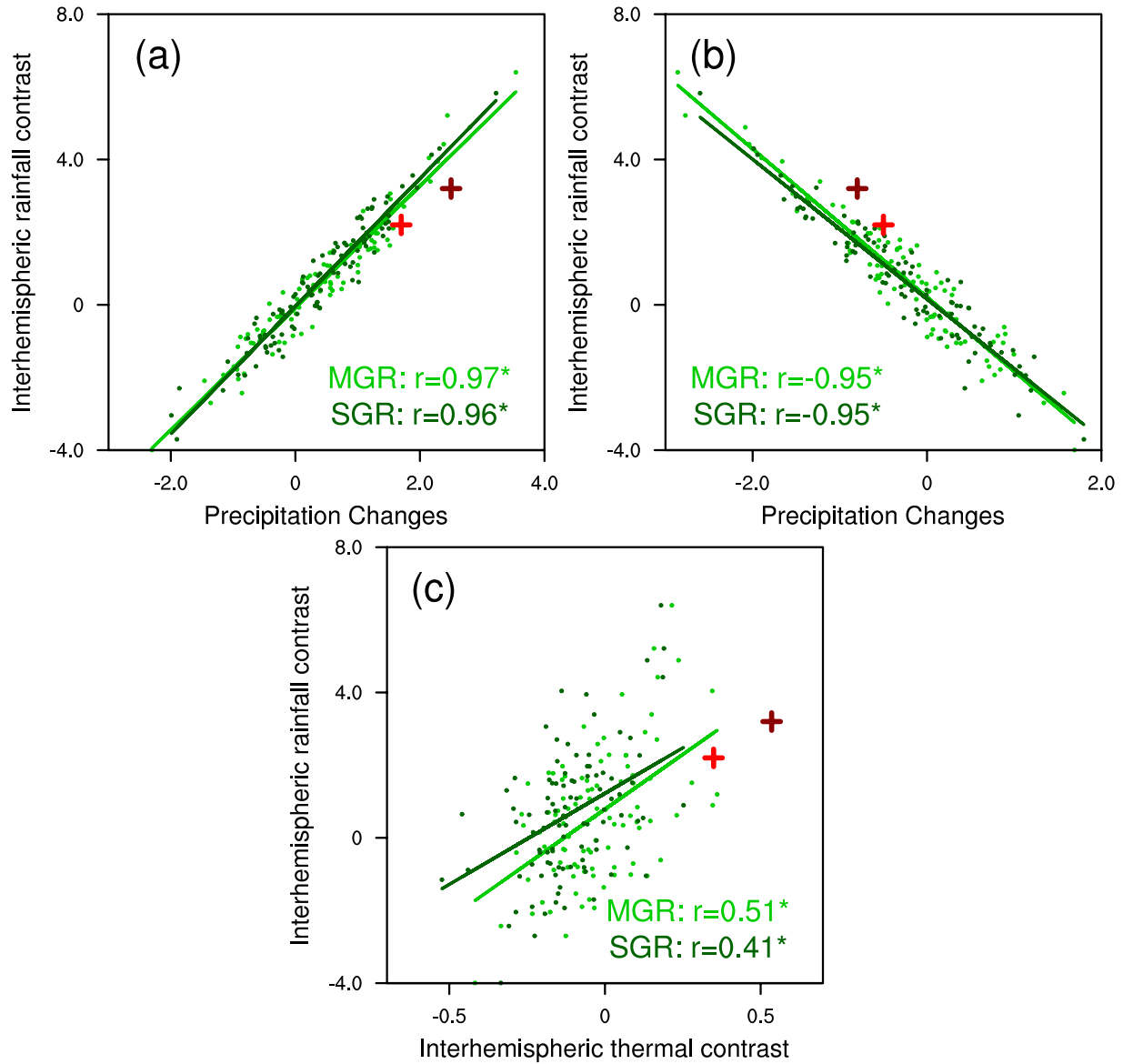
Figure 11. Scatter plots of changes in boreal summer mean interhemispheric rainfall contrast (y axis; unit: mm month^{-1}) versus (a) North Hemispheric mean and (b) South Hemispheric mean changes in boreal summer mean precipitation (x axis; unit: mm month^{-1}) in the 2040s relative to the baseline case at the same period. (c) is the same as (a) and (b) but versus changes in boreal summer mean interhemispheric thermal contrast (x axis; unit: °C). The bright green and dark green dots represent the multi-model results of the COVID-MIP models corresponding to the moderate green economic-recovery (MGR) and strong green economic-recovery (SGR) scenarios, respectively, while the bright green and dark green lines indicate the linear fits. The red and dark red plus signs represent the mean results based on CLIM_All from the BCC_AGCM2.0_CUACE/Aero simulations.

enhance the northward transport of lower-tropospheric moisture by intensifying the ITC and the resulting meridional overturning circulation, leading to an asymmetrical distribution of rainfall in boreal summer in the mid-21st century. This implies that most tropical and subtropical areas may face the risk of regional hydrological imbalance during the processes of achieving global warming mitigation and air pollution control (Allen, 2015; B. Wang et al., 2020). The precipitation changes from the BCC_AGCM2.0_CUACE/Aero simulations show consistent meridional distribution with the results recognized by the multi-model simulations from COVID-MIP, although differences in precipitation changes between these two types of simulations exist at the regional scale. These differences may arise from the uncertainty of climate models' responses to reduction in aerosol emissions (Forster et al., 2021; Hoose et al., 2009). Currently, no long-term single-forcing simulations involving only changes in

anthropogenic WMGHGs or aerosols under the green economic-recovery scenarios are available in the COVID-MIP models (Lamboll et al., 2021), and the available model outputs are also limited. More systematic analyses are needed in future work, which depend on gathering more climate model outputs and conducting more single-forcing simulations.

It should be noted that ignoring nitrate aerosol in the present work may result in slight underestimation of boreal summer rainfall (An et al., 2019; Bellouin et al., 2011; Ganguly et al., 2012); A previous study has confirmed that CMIP6 pathways have overestimated anthropogenic aerosol emissions over China since 2013, and these overestimates also exist for the COVID-MIP scenarios (Z. Wang et al., 2021). Therefore, the corresponding aerosol effect on boreal summer rainfall could be overestimated since anthropogenic aerosol emission reductions applied on percentage basis are greater than the actual condition; Note that large spreads exist among the CMIP models' projections (Chen et al., 2020; T. Zhou et al., 2020). The spread of projections is also large in the single-model ensembles, such as the interhemispheric or intertropical rainfall contrast from the BCC_AGCM2.0_CUACE/Aero simulations, which partially hampers the comparison of individual and comprehensive contributions from various anthropogenic forcings. Addressing these uncertainties will need more complex chemistry processes included, more trustworthy emission inventories, and more effective constraint techniques, in future works (An et al., 2019; Chen et al., 2022; Li et al., 2017; Z. Wang et al., 2021). Urgent mitigation actions of WMGHGs and aerosols are of course needed to limit widespread climate impacts and improve air quality (Röser et al., 2020; Z. Wang et al., 2021). In pursuing such pathways, we need to factor their specific climate response into adaptation plans to build climate resilience and pathway-appropriate adaptation policies. More in-depth analyses, such as the moisture budget analysis (Chen et al., 2020; He et al., 2020), should be considered in future work to quantify the respective contributions of thermodynamic and dynamic processes to the anthropogenic emission mitigation-induced changes in the interhemispheric precipitation asymmetricity. Responses of global monsoon rainfall (B. Wang et al., 2020), ITCZ position (Mamalakis et al., 2021), and extreme precipitation disasters (A. D. Zhao et al., 2018; Zou & Zhou, 2022) should also be further examined under the COVID-MIP green economic-recovery scenarios.

Data Availability Statement

The emission pathways for the SSP2-4.5 scenario are accessible from the InputMIPs via entering "ScenarioMIP," "emissions," and "IAMC-MESSAGE-GLOBIOM-ssp245-1-1" on the data download page (Input4MIPs, 2021; https://esgf-node.llnl.gov/search/input4mips/). The WMGHGs concentration data sets are available at https://doi.org/10.5281/zenodo.10013002 (Xie & Yu, 2023). The COVID-MIP model simulations are available through the Earth System Grid Federation by entering "DAMIP," "ssp245-cov-modgreen," and "ssp245-cov-strgreen" on the CMIP6 Search Interface (CMIP, 2021; https://esgf-node.llnl.gov/search/cmip6), while the ScenarioMIP model outputs are also accessible on the same data set platform by entering "ScenarioMIP," and "ssp245.".

References

Allan, R. P., Soden, B. J., John, V. O., Ingram, W., & Good, P. (2010). Current changes in tropical precipitation. *Environmental Research Letters*, *5*(2), 025205. https://doi.org/10.1088/1748-9326/5/2/025205

Allen, R. J. (2015). A 21st century northward tropical precipitation shift caused by future anthropogenic aerosol reductions. *Journal of Geophysical Research: Atmospheres*, *120*(18), 9087–9102. https://doi.org/10.1002/2015JD023623

Allen, R. J., Evan, A. T., & Booth, B. B. B. (2015). Interhemispheric aerosol radiative forcing and tropical precipitation shifts during the late twentieth century. *Journal of Climate*, *28*(20), 8219–8246. https://doi.org/10.1175/jcli-d-15-0148.1

An, Q., Zhang, H., Wang, Z., Liu, Y., Xie, B., Liu, Q., et al. (2019). The development of an atmospheric aerosol/chemistry-climate model, BCC_AGCM_CUACE2.0, and simulated effective radiative forcing of nitrate aerosols. *Journal of Advances in Modeling Earth Systems*, *11*(11), 3816–3835. https://doi.org/10.1029/2019MS001622

Bellouin, N., Rae, J., Jones, A., Johnson, C., Haywood, J., & Boucher, O. (2011). Aerosol forcing in the Climate Model Intercomparison Project (CMIP5) simulations by HadGEM2-ES and the role of ammonium nitrate. *Journal of Geophysical Research*, *116*(D20), D20206. https://doi.org/10.1029/2011jd016074

Bollasina, M. A., Ming, Y., Ramaswamy, V., Schwarzkopf, M. D., & Naik, V. (2011). Contribution of local and remote anthropogenic aerosols to the twentieth century weakening of the South Asian monsoon. *Geophysical Research Letters*, *41*(2), 680–687. https://doi.org/10.1002/2013GL058183

Boucher, O., Randall, D., Artaxo, P., Bretherton, C., Feingold, G., Forster, P., et al. (2013). Clouds and aerosols. In T. F. Stocker, D. Qin, G.-K. Plattner, M. Tignor, S. K. Allen, J. Boschung, et al. (Eds.), *Climate change 2013: The physical science basis. Contribution of Working Group I to the fifth assessment report of the Intergovernmental Panel on Climate Change*. Cambridge University Press.

Bracegirdle, T. J., Krinner, G., Tonelli, M., Haumann, F. A., Naughten, K. A., Rackow, T., et al. (2020). Twenty first century changes in Antarctic and Southern Ocean surface climate in CMIP6. *Atmospheric Science Letters*, *21*(9), e984. https://doi.org/10.1002/asl.984

Chen, Z., Zhou, T., Chen, X., Zhang, W., Zhang, L., Wu, M., & Zou, L. (2022). Observationally constrained projection of Afro-Asian monsoon precipitation. *Nature Communications*, *13*(1), 2552. https://doi.org/10.1038/s41467-022-30106-z

Chen, Z., Zhou, T., Zhang, L., Chen, X., Zhang, W., & Jiang, J. (2020). Global land monsoon precipitation changes in CMIP6 projections. *Geophysical Research Letters*, *47*(14), e2019GL086902. https://doi.org/10.1029/2019GL086902

Chiang, J. C., & Friedman, A. R. (2012). Extratropical cooling, interhemispheric thermal gradients, and tropical climate change. *Annual Review of Earth and Planetary Sciences*, *40*(1), 383–412. https://doi.org/10.1146/annurev-earth-042711-105545

Chou, C., Neelin, J. D., Chen, C. A., & Tu, J. Y. (2009). Evaluating the "rich-get-richer" mechanism in tropical precipitation change under global warming. *Journal of Climate*, *22*(8), 1982–2005. https://doi.org/10.1175/2008JCLI2471.1

Chou, C., Tu, J., & Tan, P. (2007). Asymmetry of tropical precipitation change under global warming. *Geophysical Research Letters*, *34*(17), L17708. https://doi.org/10.1029/2007gl030327

Chu, J., Kim, K., Lau, W. K. M., & Ha, J. (2018). How light-absorbing properties of organic aerosol modify the Asian summer monsoon rainfall? *Journal of Geophysical Research: Atmospheres*, *123*(4), 2244–2255. https://doi.org/10.1002/2017JD027642

Chung, E., & Soden, B. J. (2017). Hemispheric climate shifts driven by anthropogenic aerosol-cloud interactions. *Nature Geoscience*, *10*(8), 566–571. https://doi.org/10.1038/ngeo2988

Climate Action Tracker. (2020). A government roadmap for addressing the climate and post COVID-19 economic crises. Retrieved from https://climateactiontracker.org/publications/addressing-the-climate-and-post-covid-19-economic-crises

CMIP6. (2021). Datasets from CMIP6 simulations [Dataset]. Earth System Grid Federation. Retrieved from https://esgf-node.llnl.gov/search/cmip6/

Collins, M., Knutti, R., Arblaster, J., Dufresne, J.-L., Fichefet, T., Friedlingstein, P., et al. (2013). Long-term climate change: Projections, commitments and irreversibility. In T. F. Stocker, D. Qin, G.-K. Plattner, M. Tignor, S. K. Allen, J. Boschung, et al. (Eds.), *Climate change 2013: The physical science basis. Contribution of Working Group I to the fifth assessment report of the Intergovernmental Panel on Climate Change*. Cambridge University Press.

Cook, B. I., Seager, R., Williams, A. P., Puma, M. J., McDermid, S., Kelly, M., & Larissa, N. (2019). Climate change amplification of natural drought variability: The historic mid-twentieth-century North American drought in a warmer world. *Journal of Climate*, *32*(17), 5417–5436. https://doi.org/10.1175/JCLI-D-18-0832.1

Crippa, M., Guizzardi, D., Banja, M., Solazzo, E., Muntean, M., Schaaf, E., et al. (2022). *CO$_2$ emissions of all world countries*. JRC/IER/PBL 2022 Report. Publications Office of the European Union. https://doi.org/10.2760/07904

Deser, C., Phillips, A. S., Simpson, I. R., Rosenbloom, N., Coleman, D., Lehner, F., et al. (2020). Isolating the evolving contributions of anthropogenic aerosols and greenhouse gases: A new CESM1 large ensemble community resource. *Journal of Climate*, *33*(18), 7835–7858. https://doi.org/10.1175/JCLI-D-20-0123.1

Diao, C., Xu, Y., & Xie, S. P. (2021). Anthropogenic aerosol effects on tropospheric circulation and sea surface temperature (1980-2020): Separating the role of zonally asymmetric forcings. *Atmospheric Chemistry and Physics*, *21*(24), 18499–18518. https://doi.org/10.5194/acp-21-18499-2021

DiNezio, P. N., Vecchi, G. A., & Clement, A. C. (2013). Detectability of changes in the Walker Circulation in response to global warming. *Journal of Climate*, *26*(12), 4038–4048. https://doi.org/10.1175/JCLI-D-12-00531.1

Ding, Y., Sun, Y., Wang, Z., Zhu, Y., & Song, F. (2009). Inter-decadal variation of the summer precipitation in China and its association with decreasing Asian summer monsoon. Part II: Possible causes. *International Journal of Climatology*, *29*(13), 1926–1944. https://doi.org/10.1002/joc.1759

Ding, Y., Wang, Z., & Sun, Y. (2008). Inter-decadal variation of the summer precipitation in East China and its association with decreasing Asian summer monsoon. Part I: Observed evidences. *International Journal of Climatology*, *28*(9), 1139–1161. https://doi.org/10.1002/joc.1615

Douville, H., Raghavan, K., Renwick, J., Allan, R. P., Arias, P. A., Barlow, M., et al. (2021). Water cycle changes. In V. Masson-Delmotte, P. Zhai, A. Pirani, S. L. Connors, C. Péan, S. Berger, et al. (Eds.), *Climate change 2021: The physical science basis. Contribution of Working Group I to the sixth assessment report of the Intergovernmental Panel on Climate Change*. Cambridge University Press.

D'Souza, J., Prasanna, F., Valayannopoulos-Akrivou, L.-N., Sherman, P., Penn, E., Song, S., et al. (2021). Projected changes in seasonal and extreme summertime temperature and precipitation in India in response to COVID-19 recovery emissions scenarios. *Environmental Research Letters*, *16*(11), 114025. https://doi.org/10.1088/1748-9326/ac2f1b

Fadnavis, S., Sabin, T. P., Rap, A., Müller, R., Kubin, A., & Heinold, B. (2021). The impact of COVID-19 lockdown measures on the Indian summer monsoon. *Environmental Research Letters*, *16*(7), 074054. https://doi.org/10.1088/1748-9326/ac109c

Fiedler, S., Stevens, B., Gidden, M., Smith, S. J., Riahi, K., & van Vuuren, D. (2019). First forcing estimates from the future CMIP6 scenarios of anthropogenic aerosol optical properties and an associated Twomey effect. *Geoscientific Model Development*, *12*(3), 989–1007. https://doi.org/10.5194/gmd-12-989-2019

Forster, P. M., Forster, H. I., Evans, M. J., Gidden, M. J., Jones, C. D., Keller, C. A., et al. (2020). Current and future global climate impacts resulting from COVID-19. *Nature Climate Change*, *10*(10), 913–919. https://doi.org/10.1038/s41558-020-0883-0

Forster, P. M., Storelvmo, T., Armour, K., Collins, W., Dufresne, J.-L., Frame, D., et al. (2021). The Earth's energy budget, climate feedbacks, and climate sensitivity. In V. Masson-Delmotte, P. Zhai, A. Pirani, S. L. Connors, C. Péan, S. Berger, et al. (Eds.), *Climate change 2021: The physical science basis. Contribution of Working Group I to the sixth assessment report of the Intergovernmental Panel on Climate Change*. Cambridge University Press.

Friedlingstein, P., Jones, M. W., O'Sullivan, M., Andrew, R. M., Bakker, D. C. E., Hauck, J., et al. (2022). Global carbon budget 2021. *Earth System Science Data*, *14*(4), 1917–2005. https://doi.org/10.5194/essd-14-1917-2022

Frierson, D. M. W., & Hwang, Y. T. (2012). Extratropical influence on ITCZ shifts in slab ocean simulations of global warming. *Journal of Climate*, *25*(2), 720–733. https://doi.org/10.1175/JCLI-D-11-00116.1

Ganguly, D., Rasch, P. J., Wang, H., & Yoon, J. (2012). Climate response of the South Asian monsoon system to anthropogenic aerosols. *Journal of Geophysical Research*, *117*(D13), D13209. https://doi.org/10.1029/2012jd017508

Geng, Y. F., Xie, S. P., Zheng, X. T., & Wang, C. Y. (2020). Seasonal dependency of tropical precipitation change under global warming. *Journal of Climate*, *33*(18), 7897–7908. https://doi.org/10.1175/JCLI-D-20-0032.1

Gettelman, A., Morrison, H., & Ghan, S. J. (2008). A new two-moment bulk stratiform cloud microphysics scheme in the Community Atmosphere Model, version 3 (CAM3). Part II: Single-column and global results. *Journal of Climate*, *21*(15), 3660–3679. https://doi.org/10.1175/2008JCLI2116.1

Gong, S. L., Barrie, L. A., Blanchet, J. P., von Salzen, K., Lohmann, U., Lesins, G., et al. (2003). Canadian Aerosol Module: A size segregated simulation of atmospheric aerosol processes for climate and air quality models 1. Module development. *Journal of Geophysical Research*, *108*(D1), 4007. https://doi.org/10.1029/2001jd002002

Gong, S. L., Barrie, L. A., & Lazare, M. (2002). Canadian Aerosol Module (CAM): A size-segregated simulation of atmospheric aerosol processes for climate and air quality models 2. Global sea-salt aerosol and its budgets. *Journal of Geophysical Research*, *107*(D24), 4779. https://doi.org/10.1029/2001JD002004

Green, B., & Marshall, J. (2017). Coupling of trade winds with ocean circulation damps ITCZ shifts. *Journal of Climate*, *30*(12), 4395–4411. https://doi.org/10.1175/JCLI-D-16-0818.1

Hansen, J., Lacis, A., Rind, D., Russell, G., Stone, P., Fung, I., et al. (1984). Climate sensitivity: Analysis of feedback mechanisms. In M. Ewing, J. E. Hansenand, & T. Takahashi (Eds.), *Climate processes and climate sensitivity*. AGU Geophysical Monograph.

He, C., Li, T., & Zhou, W. (2020). Drier North American monsoon in contrast to Asian–African monsoon under global warming. *Journal of Climate*, *33*(22), 9801–9816. https://doi.org/10.1175/JCLI-D-20-0189.1

He, C., Zhou, W., Li, T., Zhou, T., & Wang, Y. (2022). East Asian summer monsoon enhanced by COVID-19. *Climate Dynamics*, *59*(9–10), 2965–2978. https://doi.org/10.1007/s00382-022-06247-8

He, J., Xie, B., Zhang, H., & Yu, X. (2022). Impacts of greenhouse gases and anthropogenic aerosols changes on surface air temperature in East Asia under different post-pandemic period emission scenarios. *Advances in Climate Change Research*, *13*(6), 884–895. https://doi.org/10.1016/j.accre.2022.10.004

Held, I. M., & Soden, B. J. (2006). Robust responses of the hydrological cycle to global warming. *Journal of Climate*, *19*(21), 5686–5699. https://doi.org/10.1175/jcli3990.1

Hepburn, C., O'Callaghan, B., Stern, N., Stiglitz, J., & Zenghelis, D. (2020). Will COVID-19 fiscal recovery packages accelerate or retard progress on climate change. *Oxford Review of Economic Policy*, *36*(Supplement_1), S359–S381. https://doi.org/10.1093/oxrep/graa015

Hoose, C., Kristjánsson, J., Iversen, T., Kirkevåg, A., Seland, Ø., & Gettelman, A. (2009). Constraining cloud droplet number concentration in GCMs suppresses the aerosol indirect effect. *Geophysical Research Letters*, *36*(12), L12807. https://doi.org/10.1029/2009gl038568

Hwang, Y., Frierson, D. M. W., & Kang, S. M. (2013). Anthropogenic sulfate aerosol and the southward shift of tropical precipitation in the late 20th century. *Geophysical Research Letters*, *40*(11), 2845–2850. https://doi.org/10.1002/grl.50502

Input4MIPs. (2021). The generation of gridded emissions data for CMIP6 [Dataset]. Earth System Grid Federation. Retrieved from https://esgf-node.llnl.gov/search/input4mips/

Jing, X., Zhang, H., Peng, J., Li, J., & Barker, H. W. (2016). Cloud overlapping parameter obtained from CloudSat/CALIPSO data set and its application in AGCM with McICA scheme. *Atmospheric Research*, *170*(15), 52–65. https://doi.org/10.1016/j.atmosres.2015.11.007

Kang, S. M. (2020). Extratropical influence on the tropical rainfall distribution. *Current Climate Change Reports*, *6*(1), 24–36. https://doi.org/10.1007/s40641-020-0015-y

Kang, S. M., Frierson, D. M. W., & Held, I. M. (2009). The tropical response to extratropical thermal forcing in an idealized GCM: The importance of radiative feedbacks and convective parameterization. *Journal of Climate*, *66*(9), 2812–2827. https://doi.org/10.1175/2009JAS2924.1

Kang, S. M., Held, I. M., Frierson, D. M. W., & Zhao, M. (2008). The response of the ITCZ to extratropical thermal forcing: Idealized slab-ocean experiments with a GCM. *Journal of Climate*, *21*(14), 3521–3532. https://doi.org/10.1175/2007jcli2146.1

Kishore, P., Basha, G., Ratnam, M. V., AghaKouchak, A., Velicogna, I., & Rajeevan, M. (2022). Precipitation variability over India during the 20th and 21st centuries: Investigating natural and anthropogenic drivers. *Climatic Change*, *172*(3–4), 1–20. https://doi.org/10.1007/s10584-021-03068-2

Kripalani, R., Ha, K., Ho, C., Oh, J., Preethi, B., Mujumdar, M., & Prabhu, A. (2022). Erratic Asian summer monsoon 2020: COVID-19 lockdown initiatives possible cause for these episodes? *Climate Dynamics*, *59*(5–6), 1339–1352. https://doi.org/10.1007/s00382-021-06042-x

Lamboll, R. D., Jones, C. D., Skeie, R. B., Fiedler, S., Samset, B. H., Gillett, P., et al. (2021). Modifying emission scenario projections to account for the effects of COVID-19: Protocol for CovidMIP. *Geoscientific Model Development*, *14*(6), 3683–3695. https://doi.org/10.5194/gmd-14-3683-2021

Lau, W. K. M., & Kim, K. M. (2015). Robust Hadley Circulation changes and increasing global dryness due to CO_2 warming from CMIP5 model projections. *Proceedings of the National Academy of Sciences*, *112*(12), 3630–3635. https://doi.org/10.1073/pnas.1418682112

Lau, W. K. M., & Kim, K. M. (2017). Competing influence of greenhouse warming and aerosols on Asian summer monsoon circulation and rainfall. *Asia-Pacific Journal of Atmospheric Sciences*, *53*(2), 181–194. https://doi.org/10.1007/s13143-017-0033-4

Lei, Y., Wang, Z., Wang, D., Zhang, X., Che, H., Yue, X., et al. (2023). Co-benefits of carbon neutrality in enhancing and stabilizing solar and wind energy. *Nature Climate Change*, *13*(7), 1–8. https://doi.org/10.1038/s41558-023-01692-7

Lei, Y., Wang, Z., Zhang, X., Che, H., Yue, X., Tian, C., et al. (2022). Avoided population exposure to extreme heat under two scenarios of global carbon neutrality by 2050 and 2060. *Environmental Research Letters*, *17*(9), 094041. https://doi.org/10.1088/1748-9326/ac8e1b

Le Quéré, C., Jackson, R. B., Jones, M. W., Smith, A. J., Abernthy, S., Andrew, R. M., et al. (2020). Temporary reduction in daily global CO_2 emissions during the COVID-19 forced confinement. *Nature Climate Change*, *10*(7), 647–653. https://doi.org/10.1038/s41558-020-0797-x

Li, G., Xie, S., He, C., & Chen, Z. (2017). Western Pacific emergent constraint lowers projected increase in Indian summer monsoon rainfall. *Nature Climate Change*, *7*(10), 708–712. https://doi.org/10.1038/nclimate3387

Liang, J., Tan, M. L., Hawcroft, M., Catto, J. L., Hodges, K. I., & Haywood, J. M. (2022). Monsoonal precipitation over Peninsular Malaysia in the CMIP6 HighResMIP experiments: The role of model resolution. *Climate Dynamics*, *58*(9–10), 2783–2805. https://doi.org/10.1007/s00382-021-06033-y

Lund, M. T., Myhre, G., & Samset, B. H. (2019). Anthropogenic aerosol forcing under the shared socioeconomic pathways. *Atmospheric Chemistry and Physics*, *19*(22), 13827–13839. https://doi.org/10.5194/acp-19-13827-2019

Mamalakis, A., Randerson, J. T., Yu, J. Y., Pritchard, M. S., Magnusdottir, G., Smyth, P., et al. (2021). Zonally contrasting shifts of the tropical rain belt in response to climate change. *Nature Climate Change*, *11*(2), 143–151. https://doi.org/10.1038/s41558-020-00963-x

Marshall, J., Donohoe, A., Ferreira, D., & McGee, D. (2014). The ocean's role in setting the mean position of the Inter-Tropical Convergence Zone. *Climate Dynamics*, *42*(7–8), 1967–1979. https://doi.org/10.1007/s00382-013-1767-z

McCollum, D. L., Zhou, W., Bertram, C., de Boer, H., Bosetti, V., Busch, S., et al. (2018). Energy investment needs for fulfilling the Paris Agreement and achieving the Sustainable Development Goals. *Nature Energy*, *3*(7), 589–599. https://doi.org/10.1038/s41560-018-0179-z

Ming, Y., & Ramaswamy, V. (2009). Nonlinear climate and hydrological responses to aerosol effects. *Journal of Climate*, *22*(6), 1329–1339. https://doi.org/10.1175/2008jcli2362.1

Monerie, P., Wilcox, L. J., & Turner, A. G. (2022). Effects of anthropogenic aerosol and greenhouses gas emissions on Northern Hemisphere monsoon precipitation: Mechanisms and uncertainty. *Journal of Climate*, *35*(8), 2305–2326. https://doi.org/10.1175/JCLI-D-21-0412.1

Morrison, H., & Gettelman, A. (2008). A new two-moment bulk stratiform cloud microphysics scheme in the Community Atmosphere Model, version 3 (CAM3). Part I: Description and numerical tests. *Journal of Climate*, *21*(15), 3642–3659. https://doi.org/10.1175/2008JCLI2105.1

Myhre, G., Samset, B. H., Schulz, M., Balkanski, Y., Bauer, S., Berntsen, T. K., et al. (2013). Radiative forcing of the direct aerosol effect from AeroCom II Phase simulations. *Atmospheric Chemistry and Physics*, *13*(4), 1853–1877. https://doi.org/10.5194/acp-13-1853-2013

Earth's Future

Nakajima, T., Tsukamoto, M., Tsushima, Y., Numaguti, A., & Kimura, T. (2000). Modeling of the radiative process in an atmospheric general circulation model. *Applied Optics*, *39*(27), 4869–4878. https://doi.org/10.1364/AO.39.004869

O'Neill, B. C., Tebaldi, C., van Vuuren, D. P., Eyring, V., Friedlingstein, P., Hurtt, G., et al. (2016). The Scenario Model Intercomparison Project (ScenarioMIP) for CMIP6. *Geoscientific Model Development*, *9*, 3461–3482. https://doi.org/10.5194/gmd-9-3461-2016

Ourdar, T., Kushner, P. J., Fyfe, J. C., & Sigmond, M. (2018). No impact of anthropogenic aerosols on early 21st century global temperature trends in a large initial-condition ensemble. *Geophysical Research Letters*, *45*(17), 9245–9252. https://doi.org/10.1029/2009GL038568

Plesca, E., Buehler, S. A., & Grützun, V. (2018). The fast response of the tropical circulation to CO_2 forcing. *Journal of Climate*, *31*(24), 9903–9920. https://doi.org/10.1175/JCLI-D-18-0086.1

Rosenfeld, D., Andreae, M. O., Asmi, A., Chin, M., de Leeuw, G., Donovan, D. P., et al. (2014). Global observations of aerosol-cloud-precipitation-climate interactions. *Reviews of Geophysics*, *52*(4), 750–808. https://doi.org/10.1002/2013RG000441

Röser, F., Widerberg, O., Höhne, N., & Day, T. (2020). Ambition in the making: Analysing the preparation and implementation process of the Nationally Determined Contributions under the Paris Agreement. *Climate Policy*, *20*(4), 415–429. https://doi.org/10.1080/14693062.2019.1708697

Samset, B., Sand, M., Smith, C. J., Bauer, S. E., Forster, P. M., Fuglestvedt, J. S., et al. (2018). Climate impacts from a removal of anthropogenic aerosol emissions. *Geophysical Research Letters*, *45*(2), 1020–1029. https://doi.org/10.1002/2017GL076079

Sanderson, B. M., O'Neill, B. C., & Tebaldi, C. (2016). What would it take to achieve the Paris temperature targets? *Geophysical Research Letters*, *43*(13), 7133–7142. https://doi.org/10.1002/2016GL069563

Schneider, T., Bischoff, T., & Haug, G. H. (2014). Migrations and dynamics of the intertropical convergence zone. *Nature*, *513*(7516), 45–53. https://doi.org/10.1038/nature13636

Singh, D. (2016). Tug of war on rainfall changes. *Nature Climate Change*, *6*(1), 20–22. https://doi.org/10.1038/nclimate2901

Soden, B. J., & Held, I. M. (2006). An assessment of climate feedbacks in coupled ocean-atmosphere models. *Journal of Climate*, *19*(14), 3354–3360. https://doi.org/10.1175/JCLI3799.1

Song, F., Zhou, T., & Qian, Y. (2014). Responses of East Asian summer monsoon to natural and anthropogenic forcings in the 17 latest CMIP5 models. *Geophysical Research Letters*, *41*(2), 596–603. https://doi.org/10.1002/2013GL058705

Tan, P. H., Chou, C., & Tu, J. Y. (2008). Mechanisms of global warming impacts on robustness of tropical precipitation asymmetry. *Journal of Climate*, *21*(21), 5585–5602. https://doi.org/10.1175/2008JCLI2154.1

United Nations Environment Programme. (2022). Emissions gap report 2022: The closing window – Climate crisis calls for rapid transformation of societies. Retrieved from https://www.unep.org/emission-gap-report-2022

Wang, B., Jin, C., & Liu, J. (2020). Understanding future change of global monsoons projected by CMIP6 models. *Journal of Climate*, *33*(15), 6471–6489. https://doi.org/10.1175/JCLI-D-19-0993.1

Wang, H., Xie, S., Kosaka, Y., Liu, Q., & Du, Y. (2019). Dynamics of Asian summer monsoon response to anthropogenic aerosol forcing. *Journal of Climate*, *32*(3), 843–858. https://doi.org/10.1175/JCLI-D-18-0386.1

Wang, H., Xie, S., & Liu, Q. (2016). Comparison of climate response to anthropogenic aerosol versus greenhouse gas forcing: Distinct patterns. *Journal of Climate*, *29*(14), 5175–5188. https://doi.org/10.1175/JCLI-D-16-0106.1

Wang, H., Xie, S., Zheng, X., Kosaka, Y., Xu, Y., & Geng, Y. (2020). Dynamics of Southern Hemisphere atmospheric circulation response to anthropogenic aerosol forcing. *Geophysical Research Letters*, *47*(19), e2020GL089919. https://doi.org/10.1029/2020GL089919

Wang, Z., Lin, L., Xu, Y., Che, H., Zhang, X., Zhang, H., et al. (2021). Incorrect Asian aerosols affecting the attribution and projection of regional climate change in CMIP6 models. *npj Climate and Atmospheric Science*, *4*(1), 1–8. https://doi.org/10.1038/s41612-020-00159-2

Wang, Z., Zhang, H., & Lu, P. (2014). Improvement of cloud microphysics in the aerosol-climate model BCC_AGCM2.0.1_CUACE/Aero, evaluation against observations, and updated aerosol indirect effect. *Journal of Geophysical Research: Atmospheres*, *119*(13), 8400–8417. https://doi.org/10.1002/2014JD021886

Wang, Z., Zhang, H., & Zhang, X. (2015). Projected response of East Asian summer monsoon system to future reductions in emissions of anthropogenic aerosols and their precursors. *Climate Dynamics*, *47*(5–6), 1455–1468. https://doi.org/10.1007/s00382-015-2912-7

Wei, L., Lu, Z., Wang, Y., Liu, X., Wang, W., Wu, C., et al. (2022). Black carbon-climate interactions regulate dust burdens over India revealed during COVID-19. *Nature Communications*, *13*(1), 1839. https://doi.org/10.1038/s41467-022-29468-1

Wentz, F. J., Ricciardulli, L., Hilburn, K., & Mears, C. (2007). How much more rain will global warming bring? *Science*, *317*(5835), 233–235. https://doi.org/10.1126/science.1140746

Westervelt, D. M., Horowitz, L. W., Naik, V., Golaz, J., & Mauzerall, D. L. (2015). Radiative forcing and climate response to projected 21st century aerosol decreases. *Atmospheric Chemistry and Physics*, *15*(22), 12681–12703. https://doi.org/10.5194/acp-15-12681-2015

Wilcox, L. J., Liu, Z., Samset, B. H., Hawkins, E., Lund, M. T., Nordling, K., et al. (2020). Accelerated increases in global and Asian summer monsoon precipitation from future aerosol reductions. *Atmospheric Chemistry and Physics*, *20*(20), 11955–11977. https://doi.org/10.5194/acp-20-11955-2020

Wu, T., Yu, R., Zhang, F., Wang, Z., Dong, M., Wang, L., et al. (2010). The Beijing Climate Center atmospheric general circulation model: Description and its performance for the present-day climate. *Climate Dynamics*, *34*(1), 123–147. https://doi.org/10.1007/s00382-008-0487-2

Xie, B., & Yu, X. (2023). The COVID19 concentration datasets [Dataset]. Zenodo. https://doi.org/10.5281/zenodo.10013002

Xu, J., Powell, A. M., Jr., & Zhao, J. (2013). Intercomparison of temperature trends in IPCC CMIP5 simulations with observations, reanalyses and CMIP3 models. *Geoscientific Model Development*, *6*(5), 1705–1714. https://doi.org/10.5194/gmd-6-1705-2013

Yang, Y., Ren, L., Li, H., Wang, H., Wang, P., Chen, L., et al. (2020). Fast climate responses to aerosol emission reductions during the COVID-19 pandemic. *Geophysical Research Letters*, *47*(19), e2020GL089788. https://doi.org/10.1029/2020GL089788

Yang, Y., Ren, L., Wu, M., Wang, H., Song, F., Leung, L. R., et al. (2022). Abrupt emissions reductions during COVID-19 contributed to record summer rainfall in China. *Nature Communications*, *13*(1), 959. https://doi.org/10.1038/s41467-022-28537-9

Yu, X., Zhang, H., Xie, B., Wang, Z., Zhao, S., Zhao, D., et al. (2022). Effective radiative forcing due to anthropogenic emission changes under Covid-19 and post-pandemic recovery scenarios. *Journal of Geophysical Research: Atmospheres*, *127*(8), e2021JD036251. https://doi.org/10.1029/2021JD036251

Zhang, H. (2016). *BCC_RAD atmosphere radiation transfer model*. Meteorological Press. (in Chinese).

Zhang, H., Chen, Q., & Xie, B. (2015). A new parameterization for ice cloud optical properties used in BCC-RAD and its radiative impact. *Journal of Quantitative Spectroscopy and Radiative Transfer*, *150*, 76–86. https://doi.org/10.1016/j.jqsrt.2014.08.024

Zhang, H., Jing, X., & Li, J. (2014). Application and evaluation of a new radiation code under McICA scheme in BCC_AGCM2.0.1. *Geoscientific Model Development*, *7*(3), 737–754. https://doi.org/10.5194/gmd-7-737-2014

Zhang, H., Shen, Z., Wei, X., & Li, Z. (2012). Comparison of optical properties of nitrate and sulfate aerosol and the direct radiative forcing due to nitrate in China. *Atmospheric Research*, *113*, 113–125. https://doi.org/10.1016/j.atmosres.2012.04.020

Zhang, H., Wang, F., Li, J., Duan, Y., Zhu, C., & He, J. (2022). Potential impact of Tonga volcano eruption on global mean surface air temperature. *Journal of Meteorological Research*, *36*, 1–5. https://doi.org/10.1007/s13351-022-2013-6

Zhang, H., Wang, Z., Wang, Z., Liu, Q., Gong, S., Zhang, X., et al. (2012). Simulation of direct radiative forcing of typical aerosols and their effects on global climate using an online AGCM-aerosol coupled model system. *Climate Dynamics*, *38*(7–8), 1675–1693. https://doi.org/10.1007/s00382-011-1141-0

Zhang, H., Zhao, S., Wang, Z., Zhang, X., & Song, L. (2016). The updated effective radiative forcing of major anthropogenic aerosols and their effects on global climate at present and in the future. *International Journal of Climatology*, *36*(12), 4029–4044. https://doi.org/10.1002/joc.4613

Zhang, L., & Li, T. (2016). Relative roles of anthropogenic aerosols and greenhouse gases in land and oceanic monsoon changes during past 156 years in CMIP5 models. *Geophysical Research Letters*, *43*(10), 5295–5301. https://doi.org/10.1002/2016GL069282

Zhang, L., & Zhou, T. (2011). An assessment of monsoon precipitation changes during 1901-2001. *Climate Dynamics*, *37*(1–2), 279–296. https://doi.org/10.1007/s00382-011-0993-5

Zhang, X., Zwiers, F. W., Hegerl, G. C., Lambert, F. H., Gillett, N. P., Solomon, S., et al. (2007). Detection of human influence on twentieth-century precipitation trends. *Nature*, *448*(7152), 461–465. https://doi.org/10.1038/nature06025

Zhao, A. D., Stevenson, D. S., & Bollasina, M. A. (2018). The role of anthropogenic aerosols in future precipitation extremes over the Asian Monsoon Region. *Climate Dynamics*, *52*(9–10), 6257–6278. https://doi.org/10.1007/s00382-018-4514-7

Zhao, S., & Suzuki, K. (2019). Differing impacts of black carbon and sulfate aerosols on global precipitation and the ITCZ location via atmosphere and ocean energy perturbations. *Journal of Climate*, *32*(17), 5567–5582. https://doi.org/10.1175/JCLI-D-18-0616.1

Zhao, S., Zhang, H., Wang, Z., & Jing, X. (2017). Simulating the effects of anthropogenic aerosols on terrestrial aridity using an aerosol-climate coupled model. *Journal of Climate*, *30*(18), 7451–7463. https://doi.org/10.1175/JCLI-D-16-0407.1

Zhao, S., Zhi, X., Zhang, H., Wang, Z., & Wang, Z. (2014). Primary assessment of the simulated climatic state using a coupled aerosol-climate model BCC_AGCM2.0.1_CAM. *Climatic & Environmental Research*, *19*(3), 265–277. (in Chinese). https://doi.org/10.3878/j.issn.1006-9585.2012.12015

Zheng, H., Kong, S., Chen, N., Yan, Y., Liu, D., Zhu, B., et al. (2020). Significant changes in the chemical compositions and sources of $PM_{2.5}$ in Wuhan since the city lockdown as COVID-19. *Science of the Total Environment*, *739*, 140000. https://doi.org/10.1016/j.scitotenv.2020.140000

Zhou, C., Gong, S., Zhang, X., Liu, H., Xue, M., Cao, G., et al. (2012). Towards the improvements of simulating the chemical and optical properties of Chinese aerosols using an online coupled model – CUACE/Aero. *Tellus Series B Chemical and Physical Meteorology*, *64*(1), 91–102. https://doi.org/10.3402/tellusb.v64i0.18965

Zhou, T., Chen, X., Dong, L., Wu, B., Man, W., Zhang, L., et al. (2014). Chinese contribution to CMIP5: An overview of five Chinese model's performances. *Journal of Meteorological Research*, *28*(4), 481–509. https://doi.org/10.1007/s13351-014-4001-y

Zhou, T., Lu, J., Zhang, W., & Chen, Z. (2020). The sources of uncertainty in the projection of global land monsoon precipitation. *Geophysical Research Letters*, *47*(15), e2020GL088415. https://doi.org/10.1029/2020GL088415

Zhou, W., Xie, S., & Yang, D. (2019). Enhanced equatorial warming causes deep-tropical contraction and subtropical monsoon shift. *Nature Climate Change*, *9*(11), 834–839. https://doi.org/10.1038/s41558-019-0603-9

Zou, L., & Zhou, T. (2022). Mean and extreme precipitation changes over China under SSP scenarios: Results from high-resolution dynamical downscaling for CORDEX East Asia. *Climate Dynamics*, *58*(3–4), 1015–1031. https://doi.org/10.1007/s00382-021-05947-x